

A Theory for Wind Work on Oceanic Mesoscales and Submesoscales

Shikhar Rai^{1,2}, J. Thomas Farrar², and Hussein Aluie^{*1,3,4}

¹Department of Mechanical Engineering, University of Rochester,
Rochester, New York, USA

²Department of Physical Oceanography, Woods Hole Oceanographic
Institution, Woods Hole, Massachusetts, USA

³Department of Mathematics, University of Rochester, Rochester, New
York, USA

⁴Laboratory for Laser Energetics, University of Rochester, Rochester, New
York, USA

Abstract

Previous studies focused primarily on wind stress being proportional to wind velocity relative to the ocean velocity, which induces a curl in wind stress with polarity opposite to the ocean mesoscale vorticity, resulting in net negative wind work. However, there remains a fundamental gap in understanding how wind work on the ocean is related to the ocean's vortical and straining motions. While it is possible to derive budgets for ocean vorticity and strain, these do not provide the energy channeled into vortical and straining motions by wind stress. An occasional misconception is that a Helmholtz decomposition can separate vorticity from strain, with the latter mistakenly regarded as being solely due to the potential flow accounting for divergent motions. In fact, strain is also an essential constituent of divergence-free (or solenoidal) flows, including the oceanic mesoscales in geostrophic balance where strain-dominated regions account for approximately half the KE. There is no existing fluid dynamics framework that relates the injection of kinetic energy by a force to how this energy is deposited into vortical and straining motions. Here, we show that winds, on average, are just as effective at damping straining motions as they are at damping vortical motions. This happens because oceanic strain induces a straining wind stress gradient (WSG), which is analogous to ocean vorticity inducing a curl in wind stress. Ocean-induced WSGs alone, whether straining or vortical, always damp ocean currents. However, our theory also reveals that a significant contribution to wind work comes from inherent wind gradients, a main component of which is due to prevailing winds of the general atmospheric circulation. We find that inherent WSGs lead to asymmetric energization of ocean weather based on the polarity of vortical and straining ocean flows.

*hussein@rochester.edu

Introduction

Atmospheric wind is the primary energy source maintaining the global ocean circulation [1]. While wind provides kinetic energy (KE) to the ocean at gyrescales $> 10^3$ km, most of the ocean’s KE resides at the “mesoscales” $O(100)$ km [2]. Mesoscales are the ocean’s weather systems [3], consisting of a seemingly amorphous tangle of vortical and straining motions (Fig. 2A and [4]). There is strong evidence that in fact winds have a net damping effect on the mesoscales —a process sometimes called “eddy-killing” [5, 6, 7, 8, 9, 10]. The process substantially modifies the KE input to the ocean [11, 12, 6, 13, 10], can weaken the ocean gyres [14], and feeds back onto the gyrescale currents such as the Gulf Stream [15] and Antarctic Circumpolar Current (ACC) [16].

To explain eddy-killing, previous studies [6, 8, 7, 17] focused primarily on wind stress $\boldsymbol{\tau}$ being proportional to wind velocity \mathbf{u}_a relative to the ocean velocity \mathbf{u} , which induces a curl in wind stress, $\nabla \times \boldsymbol{\tau}$, with polarity opposite to the ocean mesoscale vorticity $\nabla \times \mathbf{u}$, resulting in net negative wind work. However, there remains a fundamental gap in understanding how wind work on the ocean is related to the ocean’s vortical and straining motions. While it is possible to derive budgets for ocean vorticity and strain, these do not provide the energy channeled into vortical and straining motions by wind stress. An occasional misconception is that a Helmholtz decomposition can separate vorticity from strain, with the latter mistakenly regarded as being solely due to the potential flow accounting for divergent motions (see Supplementary Information, SI). In fact, strain is also an essential constituent of divergence-free (or solenoidal) flows, including the oceanic mesoscales in geostrophic balance where strain-dominated regions account for approximately half the KE (Figs. S1,S9 in SI). There is no existing fluid dynamics framework that relates the injection of KE by a force to how this energy is deposited into vortical and straining motions. This is fundamental to our understanding of eddies and how they evolve, and to our ocean weather forecasting capabilities [18, 19].

Below, we show that winds, on average, are just as effective at damping straining motions as they are at damping vortical motions. This happens because oceanic strain induces a straining wind stress gradient (WSG), which is analogous to ocean vorticity inducing a curl in wind stress. Ocean-induced WSGs alone, whether straining or vortical, always damp ocean currents. However, our theory also reveals that a significant contribution to wind work comes from inherent wind gradients, a main component of which is due to prevailing winds of the general atmospheric circulation. We find that inherent WSGs lead to asymmetric energization of ocean weather based on the polarity of vortical and straining ocean flows.

Scale physics of wind work

We probe the scale physics of air-sea momentum exchange using a coarse-graining methodology, which yields a first-principles measure of power input by wind stress $\boldsymbol{\tau}$ into the surface ocean currents \mathbf{u} at all length-scales $< \ell$ [10],

$$EP_\ell = \overline{(\boldsymbol{\tau} \cdot \mathbf{u})}_\ell - \bar{\boldsymbol{\tau}}_\ell \cdot \bar{\mathbf{u}}_\ell . \quad (1)$$

Here, EP stands for Eddy Power (small scale) and $\overline{(\dots)}_\ell$ denotes spatial filtering on the sphere [20]. More details are in Methods (see also [21, 10]). By probing different length-scales ℓ in eq. (1), it was recently shown [10] that wind work at scales smaller

than $\ell = 260$ km is negative on a global average due to eddy-killing, which has a clear seasonal cycle and is concentrated in regions with high KE such as the Gulf Stream, Kuroshio, and the ACC. Here, we shall disentangle the contribution to EP_ℓ from vortical and straining oceanic flow patterns and also from the global atmospheric circulation patterns.

Results

Leading-Order Approximation We accomplish this through an approximation of EP_ℓ in eq. (1) that is rooted in a systematic multiscale expansion due to Eyink [23]. The approximation relies on the so-called “ultraviolet scale-locality” of wind work [24, 25, 26]. Ultraviolet locality of a multiscale process such as EP_ℓ is a fundamental physical property indicating that contributions from scales $\delta < \ell$ to the process at scale ℓ decay at least as fast as a power-law of the scale disparity ratio δ/ℓ (see Methods and [27]). For EP_ℓ , ultraviolet locality is valid over scales $\ell \approx 100$ km and smaller, but not over scales larger than the mesoscale spectral peak at ≈ 300 km [2] (Fig. S10 in SI). The leading order term, \widetilde{EP}_ℓ , in the multiscale expansion yields an approximation of EP_ℓ ,

$$EP_\ell \approx \widetilde{EP}_\ell = \frac{1}{2} M_2 \ell^2 \nabla \bar{\boldsymbol{\tau}}_\ell : \nabla \bar{\mathbf{u}}_\ell, \quad (2)$$

with $M_2 = 0.4$ (see Methods for derivation). We shall demonstrate below the utility of \widetilde{EP}_ℓ for disentangling air-sea momentum exchanges due to various flow patterns. First, we present evidence that that \widetilde{EP}_ℓ is indeed an accurate proxy for EP_ℓ using data from both satellites (Fig. 1) and a high-resolution coupled general circulation model (Fig. S4 in the SI). In Figs. 1, S4, panels A and B show global maps of EP_ℓ and \widetilde{EP}_ℓ , respectively, time-averaged over the dataset record. As expected, \widetilde{EP}_ℓ provides a good approximation to EP_ℓ , with a correlation coefficient of 0.9. Panels C and D in Figs. 1, S4 show instantaneous maps of EP_ℓ and \widetilde{EP}_ℓ in the Kuroshio Extension region on Dec 13, 1999 (Fig. 1) and in the Gulf Stream region on day 10 of the first year of the model output (Fig. S4). These maps also show good spatial agreement between EP_ℓ and its approximation \widetilde{EP}_ℓ with a correlation coefficient of 0.9. Agreement between EP_ℓ with \widetilde{EP}_ℓ also holds in time: their time-series are compared in panel E of Figs. 1, S4 in the Gulf Stream and ACC regions, which exhibit the pronounced seasonality found in [10]. Furthermore, panel F of Figs. 1, S4 shows a global map of the correlation coefficient between the time-series of EP_ℓ and \widetilde{EP}_ℓ at every geographic location; the average of the correlation coefficient is very high (≥ 0.9) with a relatively small standard deviation (≈ 0.05).

Energization of Strain and Vorticity

Having established that \widetilde{EP}_ℓ can accurately approximate the full expression for wind work on the ocean’s mesoscales, we are now able to disentangle contributions from vortical and straining oceanic flow patterns. The wind work proxy can be decomposed exactly as

$$\widetilde{EP}_\ell = \underbrace{\frac{1}{2} M_2 \ell^2 \bar{\mathbf{T}}_\ell^{strn} : \bar{\mathbf{S}}_\ell}_{\widetilde{EP}^{strn}} + \underbrace{\frac{1}{2} M_2 \ell^2 (\nabla \times \bar{\boldsymbol{\tau}}_\ell) \cdot \bar{\boldsymbol{\omega}}_\ell}_{\widetilde{EP}^{vort}}. \quad (3)$$

Here, \widetilde{EP}^{strn} and \widetilde{EP}^{vort} are wind work on the ocean’s mesoscale straining ($\overline{\mathbf{S}}_\ell = (\nabla\mathbf{u}_\ell + \nabla\mathbf{u}_\ell^{\text{tr}})/2$) and vortical ($\overline{\boldsymbol{\omega}}_\ell = \nabla \times \mathbf{u}_\ell$) motions, respectively, where superscript ‘ $(\dots)^{\text{tr}}$ ’ indicates the tensor transpose. See Methods for more details. Eq. (3) shows that the ocean’s vortical motions are coupled only to the curl of the wind stress, whereas the ocean’s straining motions are coupled to the straining component of wind stress, $\overline{\mathbf{T}}_\ell^{strn} = (\nabla\overline{\boldsymbol{\tau}}_\ell + \nabla\overline{\boldsymbol{\tau}}_\ell^{\text{tr}})/2$.

Fig. 2 provides example snapshots of \widetilde{EP}^{vort} and \widetilde{EP}^{strn} in panels A and B, respectively. Both panels visualize the same streamlines of the ocean currents in a region in the north Pacific. It can be seen in Fig. 2A that \widetilde{EP}^{vort} is concentrated in vortical regions occupied by eddies, while Fig. 2B shows how \widetilde{EP}^{strn} is concentrated in strain-dominated regions outside eddies where the flow is an amorphous tangle. These panels demonstrate how our theory and the resultant relation (3) successfully decompose wind work into straining and vortical contributions. Such disentanglement cannot be accomplished properly using traditional eddy detection methods such as the Okubo-Weiss criterion [28], which is a binary designation of a geographic location as either strain-dominated or vorticity-dominated even though strain and vorticity are often collocated (Fig. S2 in the SI) and can lead to severe errors in energy transfer estimates (by more than 6 \times , see Fig. S5A versus Fig. S7A in SI). Fig. 2A reveals a striking asymmetry whereby cyclonic (anti-clockwise in the northern hemisphere, NH) vortices are damped by wind (blue, $\widetilde{EP}^{vort} < 0$), whereas anticyclonic (clockwise in NH) vortices are energized by wind (red, $\widetilde{EP}^{vort} > 0$). Fig. 2B shows an analogous effect of wind on straining motions. We now provide an explanation for this phenomenon.

Asymmetric Energization of Ocean Weather

Recent studies [6, 13, 8, 10] have highlighted the importance of wind stress variations induced by the ocean’s mesoscale vortical motions. These induced wind stress gradients (WSGs) due to the ocean’s vortical eddies are often sketched as in Fig. 2C1, which illustrates how the dependence of wind stress on wind velocity relative to the ocean velocity leads to a damping of a vortical ocean eddy even when the wind velocity itself is uniform and lacks any gradient [6, 8]. This mechanism for eddy-damping is captured by \widetilde{EP}^{vort} in eq. (3), where part of $\nabla \times \overline{\boldsymbol{\tau}}_\ell$ arises due to induced WSGs.

However, past studies have overlooked induced WSGs due to the ocean’s mesoscale straining motions. Their role is naturally revealed by \widetilde{EP}^{strn} in eq. (3), which we sketch in Fig. 2D. Fig. 2D1 illustrates how the ocean’s straining motions (green), when coupled to background winds of uniform velocity, induce a straining wind stress (Fig. 2D2) that opposes the ocean’s strain.

Our analysis provides a complete theory for how ocean current-induced WSGs always act to oppose the oceanic mesoscale flow, both vortical and straining motions, as sketched in Fig. 2C and Fig. 2D. The previously unrecognized mesoscale damping of strain is significant and accounts for approximately half of the mesoscale damping by wind shown in Fig. 1B (see Figs. S1, S9 in SI). The other half is due to the mesoscale damping of vortical motions [6, 8].

In addition to induced WSGs, our theory accounts for the effect of inherent wind gradients on oceanic mesoscales. Most previous studies analyzed wind work on the mesoscales using a Reynolds decomposition [15, 11, 13, 29], which does not incorporate

the role of inherent wind gradients. Those studies focused on analyzing the quantity $\langle \boldsymbol{\tau}' \cdot \mathbf{u}' \rangle$, where $\langle \dots \rangle$ represents a temporal or spatial average and $(\dots)'$ represents fluctuations about that average. In contrast, the quantity EP_ℓ in eq. (1), which arises from the coarse-graining framework, naturally accounts for the role of wind gradients that are inherent to the global atmospheric circulation patterns. This role of inherent WSGs appears in the $\nabla \bar{\boldsymbol{\tau}}_\ell$ factor of \widetilde{EP}_ℓ in eq. (2).

Fig. 2E-F explains how a spatially varying stress due to the prevailing winds acts on mesoscales. Panel E decomposes wind stress into a uniform (translational) stress and a shear stress. The latter can be further decomposed into vortical and straining wind stress components as shown in Fig. 2E. Panel F sketches the orientation of vortical and straining stresses from inherent gradients of the prevailing zonal (east-west) winds in the subtropics due to the atmospheric planetary circulation. Since these stresses arise from inherent spatial gradients in the prevailing winds, they do not always act to oppose the mesoscale flow, unlike WSGs induced by ocean currents.

In the subtropics, we see from Fig. 2F that the inherent WSG is anticyclonic, *i.e.* it has negative curl in the northern hemisphere (NH) and positive curl in the southern hemisphere (SH). This imparts an asymmetry to wind work on vortical motions, whereby cyclonic eddies are damped and anticyclonic eddies are energized by the subtropical prevailing winds. It explains the wind work patterns seen in Fig. 2A. Panel F in Fig. 2 shows that there is a similar asymmetry in how the prevailing winds force straining mesoscale motions.

We separate straining motions based on the angle θ made by the strain's diverging arm with the zonal (east-west) direction, which ranges from -90° to $+90^\circ$. In analogy with the curl being either positive or negative, strain can have either $\theta > 0^\circ$ or $\theta < 0^\circ$. Using this partitioning of strain, the subtropical winds in the NH/SH exert $\theta > 0^\circ / \theta < 0^\circ$ straining stress on the oceanic mesoscales.

From the preceding discussion, wind work on the mesoscales is determined by the combination of inherent and induced wind gradients. This is made precise by simplifying eq. (3) to

$$\widetilde{EP}_\ell \approx \alpha |\mathbf{u}_a| \ell^2 \left[\underbrace{\bar{\mathbf{S}}_a : \bar{\mathbf{S}} + \bar{\boldsymbol{\omega}}_a \cdot \bar{\boldsymbol{\omega}}}_{\text{inherent}} - \underbrace{(|\bar{\mathbf{S}}|^2 + |\bar{\boldsymbol{\omega}}|^2)}_{\text{induced}} \right], \quad (4)$$

where $\alpha = \rho_{air} C_D M_2 / 2$ with air density ρ_{air} and drag coefficient C_d (see Methods for details). The induced portion of wind work is negative semi-definite, damping the mesoscales. The inherent portion of wind work depends on the mesoscale flow's orientation relative to wind gradients as described in Fig. 2E-F. In regions where the mesoscales are very strong (Fig. S1C), such as in western boundary currents, the induced portion in eq. (4) is always greater than that due to inherent WSGs and eddy-damping dominates regardless of the mesoscale flow orientation. However, in the remaining 90% of the world's oceans as shown in Fig. 3, inherent WSGs play a central role. That wind work on mesoscales is the outcome of a competition between inherent and induced WSGs was not recognized before, which our theory is able to quantify via eq. (4).

Fig. 3 (and Fig. S6 in SI) reveals a markedly asymmetric wind work on mesoscales depending on their polarity. Fig. 3A shows wind work on vortical mesoscale motions with positive curl ($\widetilde{EP}_{\omega > 0}^{vort}$), which resembles the curl of wind stress ($\nabla \times \bar{\boldsymbol{\tau}}$) in Fig. 3C.

Similarly, Fig. 3B shows wind work on vortical mesoscale motions with negative curl ($\widetilde{EP}_{\omega < 0}^{vort}$), which is almost the exact opposite of that in panel A. Asymmetric wind energization by the prevailing winds may explain, at least partly, the observed asymmetry of cyclonic versus anticyclonic eddies [30, 31], and the fact that anticyclonic eddies have a longer lifetime than cyclonic eddies [32, 33].

An analogous effect exists for the mesoscale strain. We see in Fig. 3D that wind work on straining mesoscale motions having a diverging arm with angle $\theta > 0^\circ$ resembles the straining component of wind stress $((\nabla\bar{\tau}_\ell + \nabla\bar{\tau}_\ell^{tr})/2)$ in Fig. 3F. On the other hand, wind work on straining mesoscale motions with $\theta < 0^\circ$ is almost the exact opposite of that in panel D.

In Fig. 3, strongly eddying regions such as in the Gulf Stream, Kuroshio, and ACC, we see a contrasting behavior. In these regions, the induced contribution dominates in eq. (4) rendering it negative such that winds damp mesoscale motions regardless of polarity.

Without the decomposition of wind work in Figs. 3,S6 based on polarity of the ocean’s mesoscale vorticity and strain, the asymmetric energization by the prevailing winds would not be apparent. Indeed, the sum of panels A,B,D,E in Fig. 3 yields \widetilde{EP}_ℓ in Fig. 1B, which is negative almost everywhere in the global ocean. Even a decomposition of wind work on mesoscale strain and vorticity separately (Fig. S1 in SI), without distinguishing polarities, indicates that these oceanic motions are damped on average. This is because the induced WSGs contribution in eq. (4) is persistently negative regardless of the ocean flow’s orientation. When ocean weather of mixed polarity passes through any geographic location (Eulerian perspective), the imprint of inherent winds can seem significantly smaller than what the actual ocean weather system experiences (Lagrangian perspective).

Seasonality of wind work on mesoscale vorticity and strain of each polarity is shown in Figs. 3G,H at subtropical latitudes, excluding regions of strong mesoscale KE (see Methods). Magnitudes of wind work peak during winter of each hemisphere, regardless of whether wind acts to energize or dampen the mesoscales. This can be understood from eq. (4), where \widetilde{EP}_ℓ is proportional to the mesoscale strength, which peaks in spring [2], and to wind speed $|\mathbf{u}_a|$, which peaks in winter. Since absolute seasonal variations of the latter are much larger, they govern the seasonality of wind work [10].

Traditional techniques such as eddy detection [33, 34] or Okubo-Weiss [28] are poor at revealing the inherent asymmetry of energy transfer we found in Figs. 3,S6. The deficiency is demonstrated in Figs. S3,S8, especially from the energization time-series in panels [G] where wind work on anti-cyclonic flow oscillates around zero and lacks a clear seasonal cycle. In contrast, the counterpart time-series in panels [G] of Figs. 3,S6 using our theory are clearly positive and with a seasonal cycle. The deficiency is due to vorticity-dominated regions, as detected by these methods, having significant contributions from strain of either sign and vice versa, which contaminate the time-series.

Conclusion

Our theory quantifies wind work on ocean weather, which consists of an amorphous tangle of straining and vortical mesoscale motions. While previous studies [9, 10, 13, 34] focused on estimating the kinetic energy exchange between the atmosphere and the

ocean, a fundamental gap remained in understanding how such energy feeds or damps the ocean’s vortical and straining flows. Budgets for ocean vorticity and strain do not quantify energy transfer and we have been lacking a fluid dynamics framework that relates the two perspectives. We are able to derive such a relation here by using a coarse-graining approach [10] combined with insights into how disparate scales are coupled (scale-locality) [24, 27] and a multiscale expansion [23].

We found that, on average, wind damps oceanic strain at a rate equal to the damping of oceanic vorticity. The damping of strain had not been recognized before and has important implications to the formation of ocean fronts [35, 36]. Yet, underlying the damping of strain and vorticity is a marked asymmetry whereby wind energizes ocean weather with certain polarities. Such asymmetry arises because wind work is an outcome of a competition between induced and inherent wind stress gradients. The induced component of wind work is always negative and proportional to oceanic mesoscale strength, dominating in strong current regions, which occupy less than 10% of the ocean surface [10]. Wind work over the remaining 90% of the ocean surface is dominated by the inherent component of wind stress gradients, which energize ocean weather with certain polarities and may explain observed asymmetry of anti/cyclonic systems in the ocean [33]. These results reveal new energy pathways through which the atmosphere shapes ocean weather. We hope that an improved understanding of air-sea energy transfer can be integrated into predictive models. This is especially pertinent to climate models, which are often unable to resolve mesoscales accounting for over 50% of the global oceanic circulation’s KE [2].

Methods

Description of Datasets

Our results are based on two sets of data, one from satellites shown in the main text, and another from a high resolution coupled global model. The satellite dataset is for seven years (Oct 1999 to Dec 2006), which includes geostrophic ocean currents estimated from satellite altimetry (AVISO) and wind stress from QuikSCAT scatterometry, both projected onto a $0.25^\circ \times 0.25^\circ$ grid. Geostrophic currents along the equator are calculated using Lagerloef methodology [37] with the β plane approximation. Wind stress is calculated following the aerodynamic bulk parameterization [38, 39]. After masking the seasonal ice-covered regions and rain-flags, we calculate the weekly average to get the global coverage of wind stress.

Analysis in the supplementary information (SI) uses daily averaged surface currents and wind stress from a high-resolution coupled Community Earth System Model (CESM) simulation [40] over years 50 to 56 of the model’s output. The model has lateral resolution of $\approx 0.1^\circ \times 0.1^\circ$ for the ocean and $0.25^\circ \times 0.25^\circ$ for the atmosphere. For consistency with analysis of the satellite data, we mask the same seasonal ice-covered regions.

Scale Decomposition

We use the coarse-graining approach [41, 10] to study multiscale wind work. For any scale ℓ (in meters), we coarse-grain a field F using the convolution $*$ defined on the

surface of a sphere [20, 4, 42, 43, 44],

$$\overline{F}_\ell(\mathbf{x}) = G_\ell * F = \int_{\Omega} F(\mathbf{y}) G_\ell(\gamma(\mathbf{x}, \mathbf{y})) dS(\mathbf{y}) . \quad (5)$$

G_ℓ is a normalized convolution kernel, $dS(\mathbf{y})$ is the area measure on the sphere, Ω is the domain, and $\gamma(\mathbf{x}, \mathbf{y})$ is geodesic distance between any two locations \mathbf{x} and \mathbf{y} on the sphere. For any coarse field \overline{F}_ℓ , the complementary high-pass field containing scales smaller than ℓ is

$$F'_\ell = F - \overline{F}_\ell . \quad (6)$$

Following [10], the kernel we use is

$$G_\ell(\gamma) = A (0.5 - 0.5 \tanh((\gamma - \ell/2)/10.0)), \quad (7)$$

which is essentially a graded Top-Hat kernel with normalizing factor A to ensure $\int dS G_\ell = 1$.

Deriving the Wind Work Proxy

From equation (1),

$$\begin{aligned} EP_\ell &= \overline{(\boldsymbol{\tau} \cdot \mathbf{u})}_\ell - \overline{\boldsymbol{\tau}}_\ell \cdot \overline{\mathbf{u}}_\ell \\ &= \overline{((\overline{\boldsymbol{\tau}}_\ell + \boldsymbol{\tau}'_\ell) \cdot (\overline{\mathbf{u}}_\ell + \mathbf{u}'_\ell))}_\ell - \overline{(\overline{\boldsymbol{\tau}}_\ell + \boldsymbol{\tau}'_\ell)}_\ell \cdot \overline{(\overline{\mathbf{u}}_\ell + \mathbf{u}'_\ell)}_\ell \\ &= \overline{(\boldsymbol{\tau} \cdot \mathbf{u})}_\ell - \overline{(\boldsymbol{\tau})}_\ell \cdot \overline{(\mathbf{u})}_\ell + \text{terms with primes} \end{aligned} \quad (8)$$

Eq. (8) is exact. If the spectrum of each of the fields $\boldsymbol{\tau}$ and \mathbf{u} decays faster than k^{-1} over the wavenumber range $k \gtrsim \ell^{-1}$, then the terms with primes $(\dots)'$ are subdominant [45, 46, 47, 48]. These scaling conditions, which imply that EP_ℓ is ultraviolet scale-local at ℓ [24], do not necessarily require a power-law scaling, only that the spectrum decays sufficiently fast. For example, the conditions are satisfied if the spectrum decays exponentially and are violated near length-scales of the ocean's mesoscale peak ($\ell \approx 300$ km on a global average) or larger, where the spectral scaling becomes too shallow or has a positive slope at $\ell > 300$ km [2]. For the precise technical conditions, see [23], and for a discussion of the physical connection to smoothness along with examples, see [27].

Ultraviolet scale-locality of a multiscale process such as EP_ℓ is a fundamental physical property that is closely related to gauge invariance [26, 49, 50, 21]. It implies that contributions from length-scales $\delta < \ell$ to EP_ℓ decay at least as fast as $(\delta/\ell)^\sigma$ (with an exponent $\sigma > 0$) and that the dominant contribution to EP_ℓ comes from length-scales smaller by a multiplicative factor of $O(1)$ [24]. For our purposes here, ultraviolet scale-locality justifies neglecting all the $(\dots)'$ terms in equation (8),

$$EP_\ell \approx \overline{(\boldsymbol{\tau} \cdot \mathbf{u})}_\ell - \overline{(\boldsymbol{\tau})}_\ell \cdot \overline{(\mathbf{u})}_\ell . \quad (9)$$

From here, \widetilde{EP}_ℓ can be derived in a rather straightforward manner. Consider a 2-dimensional domain that is flat, for simplicity. A convolution with a symmetric kernel such as in eq. (7) can be written as

$$\overline{\mathbf{u}}_\ell(\mathbf{x}) = \int d^2\mathbf{r} G_\ell(\mathbf{r} - \mathbf{x}) \mathbf{u}(\mathbf{r}) = \int d^2\mathbf{r} G_\ell(\mathbf{r}) \mathbf{u}(\mathbf{x} + \mathbf{r}) . \quad (10)$$

An equivalent expression can be derived on the surface of a sphere, with spatial translations replaced with rotations [20]. Therefore,

$$\overline{(\mathbf{u}_\ell)}_\ell(\mathbf{x}) = \int d^2\mathbf{r} G_\ell(\mathbf{r}) \mathbf{u}_\ell(\mathbf{x} + \mathbf{r}) \quad (11)$$

$$\approx \int d^2\mathbf{r} G_\ell(\mathbf{r}) (\mathbf{u}_\ell(\mathbf{x}) + \mathbf{r} \cdot \nabla \mathbf{u}_\ell(\mathbf{x})) \quad (12)$$

$$= \mathbf{u}_\ell(\mathbf{x}) + \left(\int d^2\mathbf{r} \mathbf{r} G_\ell(\mathbf{r}) \right) \cdot \nabla \mathbf{u}_\ell(\mathbf{x}) \quad (13)$$

$$= \mathbf{u}_\ell(\mathbf{x}) . \quad (14)$$

Expression (12) follows from a first-order Taylor-series expansion. Note that a Taylor series expansion is not possible (series does not converge) for a field \mathbf{u} in eq. (10) with a power-law scaling shallower than k^{-3} , which precludes most turbulent flows, including geostrophic mesoscales and submesoscales. Otherwise, turbulence could be solved using Taylor series. Rather, in eq. (11), we are performing a Taylor expansion of \mathbf{u}_ℓ , which is smooth and is guaranteed to converge for $|\mathbf{r}| < \ell$ [23, 27]. Eq. (13) follows from the kernel being normalized, $\int d^2\mathbf{r} G_\ell(\mathbf{r}) = 1$. Eq. (14) follows from the symmetric property of the kernel, $\int dS \mathbf{r} G(\mathbf{r}) = 0$. Similarly,

$$\overline{(\boldsymbol{\tau}_\ell)}_\ell(\mathbf{x}) \approx \boldsymbol{\tau}_\ell(\mathbf{x}) \quad (15)$$

to leading order. A similar treatment of the first term in eq. (9) yields (using Einstein summation notation)

$$\begin{aligned} \overline{(\boldsymbol{\tau}_\ell \cdot \mathbf{u}_\ell)}_\ell(\mathbf{x}) & \approx \boldsymbol{\tau}_\ell \cdot \mathbf{u}_\ell + \partial_k \overline{(\tau_i)}_\ell \partial_j \overline{(u_i)}_\ell \int d^2\mathbf{r} r_k r_j G_\ell(\mathbf{r}) \end{aligned} \quad (16)$$

$$\begin{aligned} & = \boldsymbol{\tau}_\ell \cdot \mathbf{u}_\ell \\ & \quad + \partial_k \overline{(\tau_i)}_\ell \partial_j \overline{(u_i)}_\ell \frac{\delta_{kj}}{2} \ell^2 \int d^2\mathbf{r} \left| \frac{\mathbf{r}}{\ell} \right|^2 G_\ell(\mathbf{r}) \end{aligned} \quad (17)$$

$$= \boldsymbol{\tau}_\ell \cdot \mathbf{u}_\ell + \frac{1}{2} M_2 \ell^2 \partial_j \overline{(\tau_i)}_\ell \partial_j \overline{(u_i)}_\ell . \quad (18)$$

Eq. (17) follows from eq. (16) due to the kernel's symmetry, $\int dS \mathbf{r} G(\mathbf{r}) = 0$ [27]. An equivalent derivation yields the same result on the surface of a sphere. In eq. (18), the kernel's second moment $M_2 \equiv \int G_\ell(\gamma) \frac{\gamma^2}{\ell^2} dS$ depends on the kernel shape and taken to be 0.441 in our analysis at scale $\ell = 100$ km. Finally, combining eqs. (15), (18) into the key approximation (9) yields the expression for the proxy,

$$\begin{aligned} EP_\ell & \approx \overline{(\boldsymbol{\tau}_\ell \cdot \mathbf{u}_\ell)}_\ell - \overline{(\boldsymbol{\tau}_\ell)}_\ell \cdot \overline{(\mathbf{u}_\ell)}_\ell \\ & \approx \frac{1}{2} M_2 \ell^2 \partial_j \overline{(\tau_i)}_\ell \partial_j \overline{(u_i)}_\ell \equiv \widetilde{EP}_\ell. \end{aligned} \quad (19)$$

At any scale ℓ , the approximation improves with steeper spectra because of improved ultraviolet locality. Conversely, the approximation deteriorates as ℓ approaches a spectral peak (shallower spectra). This is demonstrated in Fig. S10 in the SI. That $(\boldsymbol{\tau}'_\ell \cdot \mathbf{u}'_\ell)_\ell$ in eq. (8) is subdominant to the term in eq. (9) highlights a fundamental difference between a length-scale decomposition and a Reynolds decomposition. In the latter,

$\langle \boldsymbol{\tau}' \cdot \mathbf{u}' \rangle$ is the only nonzero term in $\langle \boldsymbol{\tau} \cdot \mathbf{u} \rangle - \langle \boldsymbol{\tau} \rangle \cdot \langle \mathbf{u} \rangle$, which is the Reynolds analogue of eq. (8) (see [27, 51] for further discussion).

The wind work proxy can be decomposed exactly into energy transfer to straining and vortical ocean flows (eq. (3)),

$$\widetilde{EP}_\ell = \underbrace{\frac{1}{2} M_2 \ell^2 \overline{T_{ij}^{strn}} \overline{S_{ij}}}_{\widetilde{EP}^{strn}} + \underbrace{\frac{1}{2} M_2 \ell^2 \overline{T_{ij}^{vort}} \overline{\Omega_{ij}}}_{\widetilde{EP}^{vort}}. \quad (20)$$

Eq. (20) follows directly from the decomposition of ocean current gradients into symmetric and skew-symmetric components, $\nabla \bar{\mathbf{u}} = \partial_j \overline{(u_i)} = \overline{S_{ij}} + \overline{\Omega_{ij}}$. Here, $S_{ij} = (\partial_j u_i + \partial_i u_j)/2$ is the strain rate (symmetric) tensor, and $\Omega_{ij} = (\partial_j u_i - \partial_i u_j)/2$ is the rotation rate (skew-symmetric) tensor. The latter is related to vorticity $\boldsymbol{\omega} = \nabla \times \mathbf{u}$ through $\Omega_{ij} = -1/2(\epsilon_{ijk} \omega_k)$, where ϵ_{ijk} is the Levi-Civita permutation symbol (e.g., [52]). Similar to ocean current gradients, the wind stress gradients can be decomposed into symmetric and skew-symmetric components, $\nabla \bar{\boldsymbol{\tau}} = \partial_j \overline{(\tau_i)} = \overline{T_{ij}^{strn}} + \overline{T_{ij}^{vort}}$. Superscripts ‘strn’ and ‘vort’ denote the respective straining and vortical characters of the energy transfer in eq. (20) (and eq. (3) in main text), which does not include cross-interactions between symmetric and skew-symmetric components because their tensorial contraction vanishes identically (e.g., [52]).

From eq. (20) (or eq. (3) in main text), we can derive eq. (4) using the wind stress bulk formulation [39],

$$\boldsymbol{\tau} = \rho_{air} C_d |\mathbf{u}_a - \mathbf{u}| (\mathbf{u}_a - \mathbf{u}). \quad (21)$$

Here, $\rho_{air} \approx 1.2 \text{ kg/m}^3$ is air density and $C_d = O(10^{-3})$ is the coefficient of drag. Since wind speed is much larger than ocean current speed, typically by $O(10)$ to $O(100)$, we have $|\mathbf{u}_a - \mathbf{u}_o| \approx |\mathbf{u}_a|$. Moreover, wind speed is dominated by scales $> O(10^3)$ km [53, 54], implying a separation of scales between those of wind and ocean velocities and justifies the following approximation of the stress gradient at scales larger than $O(100)$ km (see also eqs. 24-25 in [22]):

$$\partial_j \bar{\boldsymbol{\tau}} \approx \rho_{air} C_d |\mathbf{u}_a| (\partial_j \bar{\mathbf{u}}_a - \partial_j \bar{\mathbf{u}}). \quad (22)$$

It follows from eq. (20) (or eq. (3) in main text) that

$$\widetilde{EP}_\ell \approx \alpha |\mathbf{u}_a| \ell^2 \left[\overline{\mathbf{S}_a} : \overline{\mathbf{S}} + \overline{\boldsymbol{\omega}_a} \cdot \overline{\boldsymbol{\omega}} - (|\overline{\mathbf{S}}|^2 + |\overline{\boldsymbol{\omega}}|^2) \right], \quad (23)$$

where $\alpha = \rho_{air} C_D M_2/2$.

Defining regions

Following [10], we generate masks for oceanic regions of interest for the plots in Fig. 1[E], S4[E] and Fig. S10. The equatorial region is the $\pm 8^\circ$ band, and the Southern Ocean region is the $[35^\circ - 65^\circ\text{S}]$ band. The remaining regions are irregular and are intended to select strongly eddying regions with strong currents. Specifically, the masks satisfy $\frac{1}{2} |\langle \mathbf{u}_o \rangle|^2 + \frac{1}{2} \langle |\mathbf{u}'_o|^2 \rangle > 0.1 \text{ m}^2/\text{s}^2$ in the Gulf Stream and Kuroshio, and $\frac{1}{2} |\langle \mathbf{u}_o \rangle|^2 + \frac{1}{2} \langle |\mathbf{u}'_o|^2 \rangle > 0.05 \text{ m}^2/\text{s}^2$ in the remaining regions. Subject to these thresholds, the masks lie within $[35^\circ - 70^\circ\text{S}]$ (ACC), $[15^\circ - 85^\circ\text{W}, 23^\circ - 55^\circ\text{N}]$ (Gulf Stream), $[120^\circ - 180^\circ\text{E}, 23^\circ - 50^\circ\text{N}]$ (Kuroshio), $[0^\circ - 45^\circ\text{E}, 15^\circ - 40^\circ\text{S}]$ (Agulhas), and $[40^\circ - 75^\circ\text{W}, 35^\circ - 60^\circ\text{S}]$ (Brazil-Malvinas).

Data Availability

Level 3 processed QuikSCAT wind measurements spanning the period of October 1999 to December 2006 used to calculate wind stress and can be accessed at https://data.marine.copernicus.eu/product/WIND_GLO_PHY_L3_MY_012_005/files?subdataset=cmems_obs-wind_glo_phy_my_l3-quikscat-seawinds-asc-0.25deg_P1D-i_202311 Geostrophic current data from AVISO Ssalto/Duacs daily sea level anomalies, which is distributed by Copernicus Marine Environment Monitoring Service (CMEMS), is used for ocean currents and can be accessed at <https://doi.org/10.48670/moi-00148> Daily averaged wind stress, sea surface height and ocean surface current output variables from Community Earth System Model (CESM) simulation [40] from simulation year 50 to 56 has been used for the plots in Supplementary Materials. The data can be downloaded from https://www.earthsystemgrid.org/dataset/ucar.cgd.asd.hybrid_v5_rel04_BC5_ne120_t12_pop62.ocn.proc.daily_ave.html. The processed data to produce the plots in the main text is available at <https://doi.org/10.5281/zenodo.14170158>

Code Availability

The coarse-graining FlowSieve package [55] is publicly available at <https://doi.org/10.5281/zenodo.14553091> and the post processing codes to reproduce the figures are available at <https://doi.org/10.5281/zenodo.14170158>.

References

- [1] Carl Wunsch and Raffaele Ferrari. Vertical Mixing, Energy, and the General Circulation of the Oceans. *Annual Review of Fluid Mechanics*, 36(1):281–314, January 2004.
- [2] Benjamin A Storer, Michele Buzzicotti, Hemant Khatri, Stephen M Griffies, and Hussein Aluie. Global energy spectrum of the general oceanic circulation. *Nature communications*, 13(1):5314, 2022.
- [3] Hyodae Seo, Larry W O’Neill, Mark A Bourassa, Arnaud Czaja, Kyla Drushka, James B Edson, Baylor Fox-Kemper, Ivy Frenger, Sarah T Gille, Benjamin P Kirtman, et al. Ocean mesoscale and frontal-scale ocean–atmosphere interactions and influence on large-scale climate: A review. *Journal of climate*, 36(7):1981–2013, 2023.
- [4] Michele Buzzicotti, Benjamin A Storer, Hemant Khatri, Stephen M Griffies, and Hussein Aluie. Spatio-temporal coarse-graining decomposition of the global ocean geostrophic kinetic energy. *Journal of Advances in Modeling Earth Systems*, 15(6):e2023MS003693, 2023.
- [5] William K Dewar and Glenn R Flierl. Some effects of the wind on rings. *Journal of physical oceanography*, 17(10):1653–1667, 1987.
- [6] Xiaoming Zhai and Richard J Greatbatch. Wind work in a model of the northwest atlantic ocean. *Geophysical research letters*, 34(4), 2007.
- [7] Hyodae Seo, Arthur J Miller, and Joel R Norris. Eddy–wind interaction in the california current system: Dynamics and impacts. *Journal of Physical Oceanography*, 46(2):439–459, 2016.
- [8] Lionel Renault, M Jeroen Molemaker, James C McWilliams, Alexander F Shchepetkin, Florian Lemarié, Dudley Chelton, Serena Illig, and Alex Hall. Modulation of wind work by oceanic current interaction with the atmosphere. *Journal of Physical Oceanography*, 46(6):1685–1704, 2016.

- [9] Lionel Renault, James C McWilliams, and Sebastien Masson. Satellite observations of imprint of oceanic current on wind stress by air-sea coupling. *Scientific reports*, 7(1):17747, 2017.
- [10] Shikhar Rai, Matthew Hecht, Matthew Maltrud, and Hussein Aluie. Scale of oceanic eddy killing by wind from global satellite observations. *Science Advances*, 7(28):eabf4920, 2021.
- [11] Thomas HA Duhaut and David N Straub. Wind stress dependence on ocean surface velocity: Implications for mechanical energy input to ocean circulation. *Journal of physical oceanography*, 36(2):202–211, 2006.
- [12] Yongsheng Xu and Robert B Scott. Subtleties in forcing eddy resolving ocean models with satellite wind data. *Ocean Modelling*, 20(3):240–251, 2008.
- [13] Chris W Hughes and Chris Wilson. Wind work on the geostrophic ocean circulation: An observational study of the effect of small scales in the wind stress. *Journal of Geophysical Research: Oceans*, 113(C2), 2008.
- [14] Andrew Mc C Hogg, William K Dewar, Pavel Berloff, Sergey Kravtsov, and David K Hutchinson. The effects of mesoscale ocean–atmosphere coupling on the large-scale ocean circulation. *Journal of Climate*, 22(15):4066–4082, 2009.
- [15] Lionel Renault, M Jeroen Molemaker, Jonathan Gula, Sebastien Masson, and James C McWilliams. Control and stabilization of the gulf stream by oceanic current interaction with the atmosphere. *Journal of Physical Oceanography*, 46(11):3439–3453, 2016.
- [16] David K Hutchinson, Andrew Mc C Hogg, and Jeffrey R Blundell. Southern ocean response to relative velocity wind stress forcing. *Journal of Physical Oceanography*, 40(2):326–339, 2010.
- [17] Véra Oerder, François Colas, Vincent Echevin, Sébastien Masson, and Florian Lemarié. Impacts of the mesoscale ocean-atmosphere coupling on the peru-chile ocean dynamics: The current-induced wind stress modulation. *Journal of Geophysical Research: Oceans*, 123(2):812–833, 2018.
- [18] EW Blockley, MJ Martin, AJ McLaren, AG Ryan, J Waters, DJ Lea, I Mirouze, KA Peterson, A Sellar, and D Storkey. Recent development of the met office operational ocean forecasting system: an overview and assessment of the new global foam forecasts. *Geoscientific Model Development*, 7(6):2613–2638, 2014.
- [19] PA Francis, AK Jithin, JB Effy, Abhisek Chatterjee, Kunal Chakraborty, A Paul, B Balaji, SSC Shenoi, P Biswamoy, Arnab Mukherjee, et al. High-resolution operational ocean forecast and reanalysis system for the indian ocean. *Bulletin of the American Meteorological Society*, 101(8):E1340–E1356, 2020.
- [20] Hussein Aluie. Convolutions on the sphere: commutation with differential operators. *GEM-International Journal on Geomathematics*, 10(1):9, 2019.
- [21] Hussein Aluie, Matthew Hecht, and Geoffrey K Vallis. Mapping the energy cascade in the north atlantic ocean: The coarse-graining approach. *Journal of Physical Oceanography*, 48(2):225–244, 2018.
- [22] Shikhar Rai, Matthew W Hecht, Mathew E Maltrud, and Hussein Aluie. Scale-dependent air-sea mechanical coupling: Resolution mismatch and spurious eddy-killing. *ESS Open Archive*, 2023.
- [23] Gregory L Eyink. Multi-scale gradient expansion of the turbulent stress tensor. *Journal of Fluid Mechanics*, 549:159–190, 2006.
- [24] Gregory L Eyink. Locality of turbulent cascades. *Physica D: Nonlinear Phenomena*, 207(1-2):91–116, 2005.
- [25] Gregory L Eyink and Hussein Aluie. Localness of energy cascade in hydrodynamic turbulence. I. Smooth coarse graining. *Physics of Fluids*, 21(11):115107, 2009.

- [26] Hussein Aluie and Gregory L Eyink. Localness of energy cascade in hydrodynamic turbulence. II. Sharp spectral filter. *Physics of Fluids*, 21(11), 2009.
- [27] Hussein Aluie, Shikhar Rai, Hao Yin, Aarne Lees, Dongxiao Zhao, Stephen M Griffies, Alistair Adcroft, and Jessica K Shang. Effective drift velocity from turbulent transport by vorticity. *Physical Review Fluids*, 7(10):104601, 2022.
- [28] John Weiss. The dynamics of enstrophy transfer in two-dimensional hydrodynamics. *Physica D: Nonlinear Phenomena*, 48(2-3):273–294, 1991.
- [29] Robert B Scott and Yongsheng Xu. An update on the wind power input to the surface geostrophic flow of the world ocean. *Deep Sea Research Part I: Oceanographic Research Papers*, 56(3):295–304, 2009.
- [30] Allen C Kuo and Lorenzo M Polvani. Nonlinear geostrophic adjustment, cyclone/anticyclone asymmetry, and potential vorticity rearrangement. *Physics of fluids*, 12(5):1087–1100, 2000.
- [31] Alexandre Stegner, Briac Le Vu, Franck Dumas, M Ali Ghannami, Amandine Nicolle, C Durand, and Y Faugere. Cyclone-anticyclone asymmetry of eddy detection on gridded altimetry product in the mediterranean sea. *Journal of Geophysical Research: Oceans*, 126(9):e2021JC017475, 2021.
- [32] Dudley B Chelton, Michael G Schlax, Roger M Samelson, and Roland A de Szoeke. Global observations of large oceanic eddies. *Geophysical Research Letters*, 34(15), 2007.
- [33] Dudley B Chelton, Michael G Schlax, and Roger M Samelson. Global observations of nonlinear mesoscale eddies. *Progress in oceanography*, 91(2):167–216, 2011.
- [34] Chi Xu, Xiaoming Zhai, and Xiao-Dong Shang. Work done by atmospheric winds on mesoscale ocean eddies. *Geophysical Research Letters*, 43(23):12–174, 2016.
- [35] Brian J Hoskins. The mathematical theory of frontogenesis. *Annual review of fluid mechanics*, 14(1):131–151, 1982.
- [36] James C. McWilliams. Oceanic frontogenesis. *Annual Review of Marine Science*, 13(Volume 13, 2021):227–253, 2021.
- [37] Gary SE Lagerloef, Gary T Mitchum, Roger B Lukas, and Pearn P Niiler. Tropical pacific near-surface currents estimated from altimeter, wind, and drifter data. *Journal of Geophysical Research: Oceans*, 104(C10):23313–23326, 1999.
- [38] WG Large and S Pond. Open ocean momentum flux measurements in moderate to strong winds. *Journal of physical oceanography*, 11(3):324–336, 1981.
- [39] William G Large, James C McWilliams, and Scott C Doney. Oceanic vertical mixing: A review and a model with a nonlocal boundary layer parameterization. *Reviews of Geophysics*, 32(4):363–403, 1994.
- [40] R Justin Small, Julio Bacmeister, David Bailey, Allison Baker, Stuart Bishop, Frank Bryan, Julie Caron, John Dennis, Peter Gent, Hsiao-ming Hsu, et al. A new synoptic scale resolving global climate simulation using the community earth system model. *Journal of Advances in Modeling Earth Systems*, 6(4):1065–1094, 2014.
- [41] Massimo Germano. Turbulence: the filtering approach. *Journal of Fluid Mechanics*, 238:325–336, 1992.
- [42] Benjamin A Storer, Michele Buzzicotti, Hemant Khatri, Stephen M Griffies, and Hussein Aluie. Global cascade of kinetic energy in the ocean and the atmospheric imprint. *Science Advances*, 9(51):eadi7420, 2023.
- [43] Hemant Khatri, Stephen M Griffies, Benjamin A Storer, Michele Buzzicotti, Hussein Aluie, Maike Sonnewald, Raphael Dussin, and Andrew Shao. A scale-dependent analysis of the barotropic vorticity budget in a global ocean simulation. *Journal of Advances in Modeling Earth Systems*, 16(6):e2023MS003813, 2024.

- [44] Salah Kouhen, Benjamin A Storer, Hussein Aluie, David P Marshall, and Hannah M Christensen. Convective and orographic origins of the mesoscale kinetic energy spectrum. *Geophysical Research Letters*, 51(21):e2024GL110804, 2024.
- [45] Hussein Aluie. Compressible turbulence: the cascade and its locality. *Physical review letters*, 106(17):174502, 2011.
- [46] Hussein Aluie, Shengtai Li, and Hui Li. Conservative cascade of kinetic energy in compressible turbulence. *The Astrophysical Journal Letters*, 751(2):L29, 2012.
- [47] Hussein Aluie. Scale decomposition in compressible turbulence. *Physica D: Nonlinear Phenomena*, 247(1):54–65, 2013.
- [48] Dongxiao Zhao, Riccardo Betti, and Hussein Aluie. Scale interactions and anisotropy in rayleigh–taylor turbulence. *Journal of Fluid Mechanics*, 930, 2022.
- [49] Hussein Aluie and Gregory L Eyink. Scale locality of magnetohydrodynamic turbulence. *Physical review letters*, 104(8):081101, 2010.
- [50] Hussein Aluie. Coarse-grained incompressible magnetohydrodynamics: analyzing the turbulent cascades. *New Journal of Physics*, 19(2):025008, 2017.
- [51] Dongxiao Zhao and Hussein Aluie. Measuring scale-dependent shape anisotropy by coarse-graining: Application to inhomogeneous rayleigh-taylor turbulence. *Physical Review Fluids*, 8(11):114601, 2023.
- [52] Rutherford Aris. *Vectors, tensors and the basic equations of fluid mechanics*. Courier Corporation, 2012.
- [53] GD Nastrom, KS Gage, and WH Jasperson. Kinetic energy spectrum of large-and mesoscale atmospheric processes. *Nature*, 310(5972):36–38, 1984.
- [54] Bel Helen Burgess, Andre R Erler, and Theodore G Shepherd. The troposphere-to-stratosphere transition in kinetic energy spectra and nonlinear spectral fluxes as seen in ecmwf analyses. *Journal of the atmospheric sciences*, 70(2):669–687, 2013.
- [55] Benjamin A Storer and Hussein Aluie. Flowsieve: A coarse-graining utility for geophysical flows on the sphere. *Journal of Open Source Software*, 8(84):4277, 2023.
- [56] Akira Okubo. Horizontal dispersion of floatable particles in the vicinity of velocity singularities such as convergences. In *Deep sea research and oceanographic abstracts*, volume 17, pages 445–454. Elsevier, 1970.

Acknowledgements We thank Hyodae Seo and Susan Wijffels for helpful discussions. This research was funded by US NASA grant 80NSSC18K0772 and US NSF grant OCE-2123496. HA was also supported by US DOE grants DE-SC0020229, DE-SC0014318, and DE-SC0019329, US NSF grants PHY-2020249 and PHY-2206380, and US NNSA grants DE-NA0003856, DE-NA0003914, DE-NA0004134. SR was also supported by NOAA grant NA22OAR4310598. JTF was supported by NASA grants 80NSSC23K098, 80NSSC19K1256, and 80NSSC21K0713. Computing time was provided by the National Energy Research Scientific Computing Center (NERSC) under Contract No. DE-AC02-05CH11231, NASA’s High-End Computing (HEC) Program through the NASA Center for Climate Simulation (NCCS) at Goddard Space Flight Center, and the Texas Advanced Computing Center (TACC) under ACCESS allocation grant EES220052.

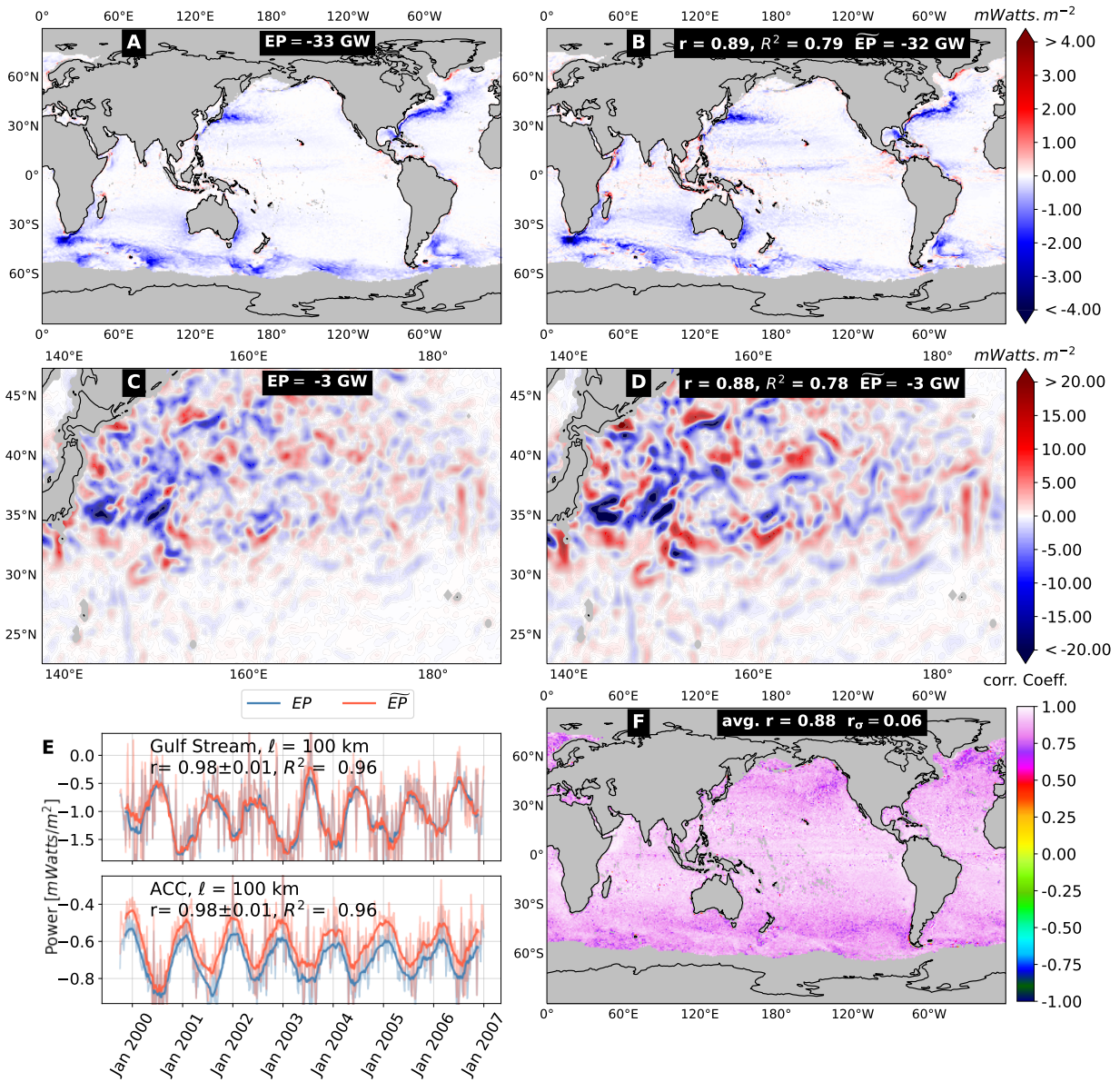


Fig. 1: Measuring Wind Energization of Ocean Weather via \overline{EP} , which is an excellent proxy for EP and affords us insight into the roles of mesoscale vortical and straining motions comprising ocean weather. [A] and [B] compare EP and \overline{EP} (averaged from Oct 1999 to Dec 2006) at $l = 100$ km using satellite data. [C] and [D] compare EP and \overline{EP} on a single day (Dec 13, 1999) in the Kuroshio Extension region. These panels demonstrate that EP in [A],[C] can be accurately approximated by \overline{EP} in [B],[D], which display a high Pearson correlation coefficient $r \approx 0.9$ and coefficient of determination $R^2 \approx 0.9$. [A]-[D] also display the area-integrated values of EP or \overline{EP} (in GigaWatts, GW). [E] shows time series of EP and \overline{EP} in the Gulf Stream and in the ACC, which again exhibit high correlation ($r = 0.98$) and demonstrates that \overline{EP} captures the seasonality of EP reported recently [10, 22]. [F] is a global map of the temporal correlation between EP and \overline{EP} at every location, and shows that $r = 0.88 \pm 0.06$, which reinforces our treatment of \overline{EP} as an accurate proxy for EP .

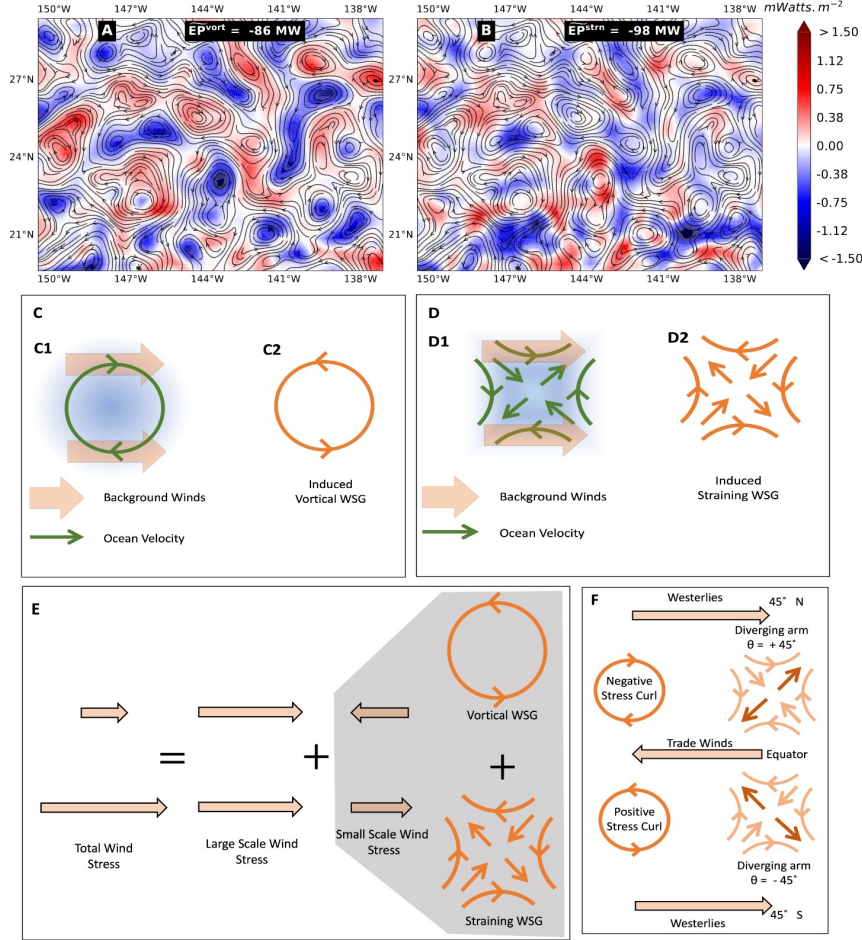


Fig. 2: Disentangling Ocean Weather Energization by Winds. Energy transfer (in Mega Watts, MW) from atmospheric winds into ocean [A] vorticity, \widetilde{EP}^{vort} and [B] strain, \widetilde{EP}^{strn} , can be analyzed for the first time using our theory and are shown here in a region in the north Pacific on Dec 6, 1999. Streamlines in [A] and [B] are identical and visualize the ocean surface currents. While vortical and straining motions always co-exist at every location, some regions can be dominated by one or the other. Demonstrating our approach, [A] shows that wind work on vorticity is most pronounced inside ocean eddies (closed streamline contours), whereas [B] shows that wind work on strain has comparable magnitude but dominates in regions outside eddies where the flow is an amorphous tangle. [C] and [D] describe the mechanisms of current-induced wind stress gradients (WSGs), which always oppose ocean currents, thereby damping both ocean vorticity and strain. In [C1], when ocean vortical flow \mathbf{u} (green) encounters uniform background winds \mathbf{u}_a , it experiences stress proportional to the relative wind velocity $\mathbf{u}_a - \mathbf{u}$, which induces a curl in wind stress (vortical WSG) that always opposes the ocean eddy [C2]. [C1] differs from the usual sketch of eddy-killing (e.g., [6, 10]) by scale-decomposing the relative wind stress, as in [E], into a sum of spatially uniform stress and smaller-scale shearing stress: the former can only lead to bulk motion but cannot transfer energy to/from ocean vortical or straining flows, which is done by the latter. In [D1], similar to [C1], when ocean strain (green) encounters uniform winds, it induces a straining WSG that always opposes the ocean strain [D2]. Ocean-induced WSGs [C,D] alone always damp ocean currents and do not explain the positive wind work (red) in [A] and [B]. This is explained by inherent wind gradients, which naturally arise in our theory, with an important component being due to the prevailing trade winds and westerlies sketched in [F]. These lead to asymmetric energization of ocean weather based on the polarity of vortical (anti/cyclonic) and straining (positive/negative angle θ) flows.

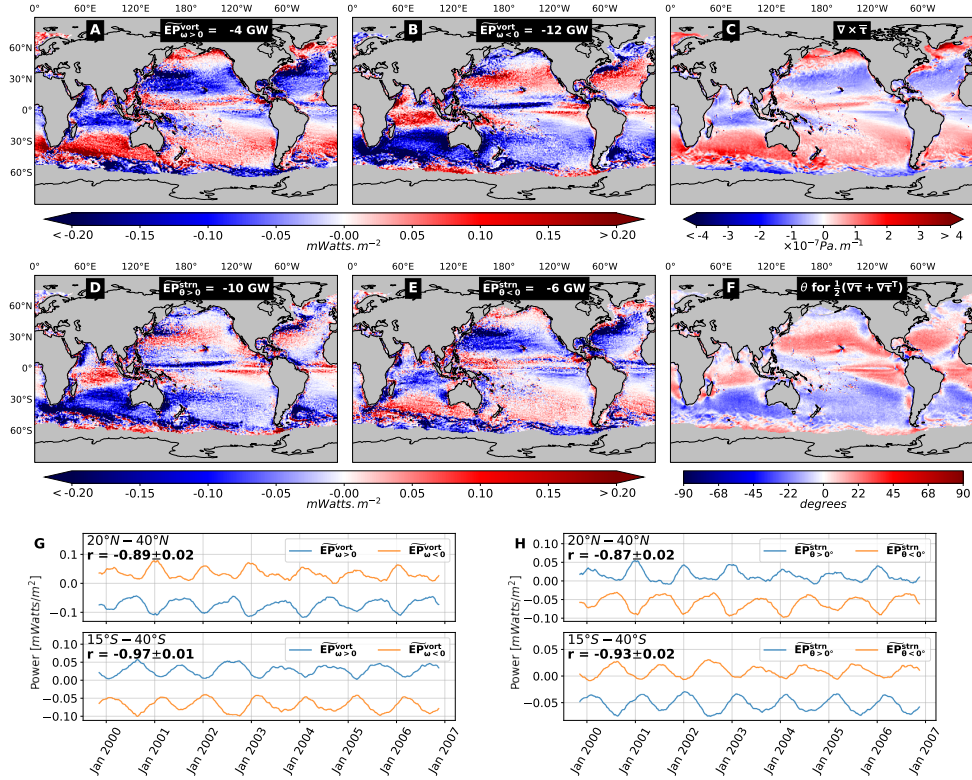


Fig. 3: Unravelling Inherent Asymmetry of Energy Transfer from Winds to Ocean Weather. Top/Bottom row shows the inherent asymmetry in wind energization of vortical/straining ocean mesoscale flows. [A]/[B] is wind work on flows with positive/negative (anti/clockwise) vorticity, which are cyclonic/anticyclonic in the northern hemisphere (NH) and anti/cyclonic in the southern hemisphere (SH). In the subtropics ($[15^\circ - 45^\circ]$), cyclonic/anticyclonic vortices are damped/energized (blue/red) by winds and the reverse occurs in sub-polar regions. While eddy-damping dominates on a global average (Fig. 1A-B), anticyclonic vortical flows are in fact energized due to inherent wind stress gradients (WSGs) in most of the subtropical oceans, except in strong current regions where the eddies are sufficiently strong such that induced WSGs, which always oppose ocean currents, dominate. [C] is a map of the time-mean wind stress curl component of inherent WSGs acting on the ocean’s mesoscales. Comparing [A-B] to [C] demonstrates the prevailing winds’ imprint (see Fig. 2F) on the ocean’s mesoscale vortical flow. Similar to vortical flows, [D-E] show wind energization of straining ocean flows with a positive/negative polarity ([D]/[E]) based on the angle θ of the local strain’s diverging arm (Fig. 2F). [F] is the time-mean angle of the straining WSG, which again demonstrates the prevailing winds’ imprint (see Fig. 2F) on the ocean’s mesoscale straining flow. [G] is a (13 weeks running mean) time series of energization of flows with positive/negative vorticity (blue/orange) at latitudes $20^\circ N - 40^\circ N$ and $15^\circ S - 40^\circ S$, excluding strong current regions where damping by induced WSGs dominates (see Methods and [10]). There is clear seasonality in [G] with the vortical flow’s energization/damping peaking during the local winter. [H] is similar to [G] but for the straining mesoscale ocean flow, which shows much the same seasonality. In [G-H], the correlation coefficients $r \leq -0.9$ between blue and orange plots of each sub-panel highlights the strong temporal correlation of asymmetric wind energization/damping of ocean weather with opposite polarity. Coarse-graining in [A-H] is at scale $\ell = 100$ km.

Supplementary Information

Strain in Divergence-free Flows

An occasional misconception is that strain is solely due to the potential flow component, $\nabla\phi$, which accounts for convergence/divergence. In fact, strain is also an essential constituent of divergence-free (or solenoidal) flows. Consider the Helmholtz decomposition of a 2-dimensional velocity field,

$$\mathbf{u} = \underbrace{\nabla\phi}_{\substack{\text{accounts for} \\ \text{strain only,} \\ \text{incl. divergence}}} + \underbrace{\nabla\times(\psi\hat{\mathbf{n}})}_{\substack{\text{divergence-free,} \\ \text{accounts for both} \\ \text{vorticity and strain}}}, \quad (\text{S-1})$$

where ψ is a streamfunction and $\hat{\mathbf{n}}$ is the unit vector normal to the flow plane. The streamfunction ψ can be proportional to sea-surface height in a geostrophic flow, for example, such as that from satellite altimetry we analyze in the paper. To see how the divergence-free component $\nabla\times(\psi\hat{\mathbf{n}})$ accounts for strain, consider its symmetric gradient,

$$\frac{1}{2}\nabla[\nabla\times(\psi\hat{\mathbf{n}})] + \frac{1}{2}\nabla[\nabla\times(\psi\hat{\mathbf{n}})]^{\text{tr}} = \begin{pmatrix} \partial_x\partial_y\psi & \frac{1}{2}(\partial_y\partial_y\psi - \partial_x\partial_x\psi) \\ \frac{1}{2}(\partial_y\partial_y\psi - \partial_x\partial_x\psi) & -\partial_x\partial_y\psi \end{pmatrix}. \quad (\text{S-2})$$

The strain in eq. (S-2) is generally non-zero almost everywhere in the flow and is dominant in saddle regions between vortices [28]. The strain tensor in eq. (S-2) is traceless, reflecting the divergence-free nature of the velocity component $\nabla\times(\psi\hat{\mathbf{n}})$ in eq. (S-1).

Wind Work on Vorticity and Strain

Okubo-Weiss Analysis

A common method to decompose flow into strain and vorticity is based on the Okubo-Weiss parameter [28],[56],

$$O = s_n^2 + s_\gamma^2 - \omega^2, \quad (\text{S-3})$$

where $s_n = \partial_x u_x - \partial_y u_y$ is proportional to the diagonal components of the deviatoric (traceless) strain rate tensor, $s_\gamma = \partial_x u_y + \partial_y u_x$ is proportional to the shear strain rate components, and relative vorticity $\omega = \partial_x u_y - \partial_y u_x$ is proportional to the components of the rotation rate tensor. The Okubo-Weiss parameter can be evaluated at any location \mathbf{x} . If $O > 0$, the location is classified as strain-dominated. If $O < 0$, the location is classified as vorticity-dominated. Therefore, the classification is binary and does not account for the co-existence of strain and vorticity at every location.

Using the Okubo-Weiss parameter, the mesoscale wind work in eq. (1) can be partitioned into wind work on vorticity-dominated regions, EP^{vort} , and wind work on strain-dominated regions, EP^{strn} . Maps of EP^{vort} and EP^{strn} are shown in Fig. S2 using satellite data and in Fig. S7 using CESM model data. When compared to Figs. 2 and Fig. S5 using our multiscale approach, we can see that on one hand, Figs. S2,S7 are qualitatively consistent, which offers support to our approach. On the other hand, Figs. S2,S7 highlight shortcomings of traditional approaches based on pattern detection. We can see that maps in Figs. S2,S7 are washed out (zero wind work) due to

the binary nature of the Okubo-Weiss criterion described above. This is because if, for example, a region is classified as strain-dominated within the Okubo-Weiss approach, wind work on vorticity is necessarily zero even though significant vorticity can be present in that region (albeit subdominant to strain). This can lead to severe errors in the bulk energy transfer estimates, which are especially pronounced in model data (Fig. S5A versus Fig. S7A) where damping estimated from Okubo-Weiss is a mere 15% of the damping revealed by our approach. Another important shortcoming of pattern detection approaches, such as Okubo-Weiss, is the inherent difficulty of deriving budgets governing coherent structures. This difficulty stems from the fact that the mask used to partition the flow into different structures is itself an implicit (and complex) function of the flow.

Similar to our approach in the main text, vorticity-dominated regions can be further partitioned into those with positive and negative vorticity. Wind work on these respective regions is then $EP_{\zeta>0}^{vort}$ and $EP_{\zeta<0}^{vort}$. Strain-dominated regions can also be partitioned into those with positive and negative strain based on the angle θ of the diverging arm of the local strain as done in the main text (see Fig. 2F). Maps of $EP_{\zeta>0}^{vort}$, $EP_{\zeta<0}^{vort}$, $EP_{\theta>0}^{strn}$ and $EP_{\theta<0}^{strn}$ based on Okubo-Weiss are shown in Figs. S3,S8 using satellite and model datasets, respectively.

When compared to their corresponding Figs. 3,S6 using our multiscale approach, Figs. S3,S8 highlight how poor Okubo-Weiss is at detecting the inherent asymmetry of energy transfer. Panels in Figs. S3,S8 are washed out due to the binary nature of the Okubo-Weiss. This is clear from the energization time-series in panels [G], where negative vorticity in the NH (orange) and positive vorticity in the SH (blue) oscillate around zero in contrast to the corresponding plots in Figs. 3,S6 which are clearly positive and indicate energization of anticyclonic flow by winds in the subtropics. Also missing from panels [G-H] is the regular seasonal signal we see clearly in Figs. 3,S6 along with a significantly weaker correlation coefficients r . This is because a vorticity-dominated region as detected by Okubo-Weiss can also have significant contributions from strain of either sign and vice versa, which contaminate the time-series.

Results from CESM

Our results from satellite data are reinforced by data from high resolution fully coupled Community Earth System Model (CESM) simulation [40]. The simulation is a 100-year run of fully coupled simulation with the atmospheric component modeled on a $\approx 0.25^\circ$ grid and the ocean component on a $\approx 0.1^\circ$ grid. The atmospheric component is the Community Atmosphere Model (CAM5) version 5 with Spectral Element (SE) dynamical core, and the ocean component is the Parallel Ocean Program (POP2). Further simulation details can found in [40]. Daily averaged wind stress and sea surface height (SSH) output variables from simulation years 50 to 56 have been used in this work. Geostrophic ocean surface currents were calculated using SSH outside $\pm 3^\circ$.

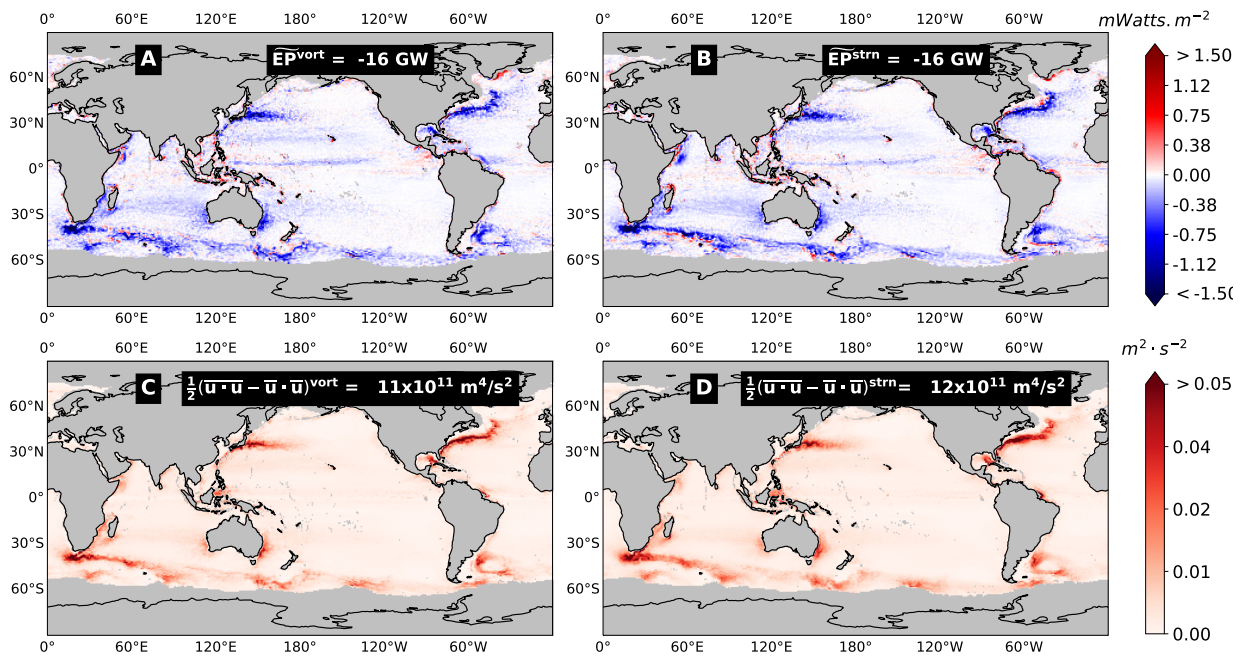


Fig. S1: Wind damping of mesoscale strain and vorticity. [A] and [B] decompose \widetilde{EP} in Fig. 1B into wind work on mesoscale [A] vorticity and [B] strain. Panels show the time average (Oct. 1999 to Dec. 2006) using satellite data as in Fig. 1. [C] and [D] show mesoscale kinetic energy at scales $\ell < 100$ km for vorticity-dominated regions and strain-dominated regions. The vorticity and strain dominated regions are masked using Okubo-Weiss parameter. This figure shows that, on average, wind damps mesoscale strain and vorticity equally and that it is most pronounced in regions with high mesoscale kinetic energy.

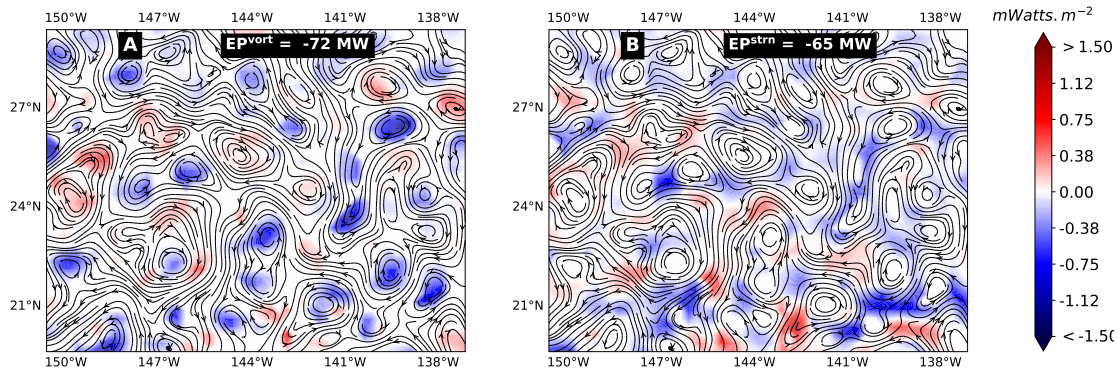


Fig. S2: Using Okubo-Weiss to decompose energy transfer to vorticity and strain. Similar to Fig. 2A-B, but using the Okubo-Weiss criterion [28] to partition the flow into [A] vorticity and [B] strain regions using a mask function. After calculating EP_ℓ from eq. (1), the mask projects EP_ℓ onto [A] vorticity-dominated and [B] strain-dominated regions. On one hand, this figure provides support to our approach by showing results that are qualitatively consistent with Fig. 2A-B. However, the figure here also highlights shortcomings of traditional approaches based on eddy detection. First, the Okubo-Weiss criterion is a binary designation of a geographic location as either strain-dominated or vorticity-dominated even though strain and vorticity are often collocated. This is manifested as washed out white regions (zero wind work) in either [A] or [B], wherever there is a colored (non-zero wind work) in the other panel at the same location. This can lead to significant errors in bulk energy transfer estimates, which are especially pronounced in model data (Fig. S5A vs Fig. S7A) where damping estimated from Okubo-Weiss is a mere 15% of the damping revealed by our approach. Second, and more importantly, it is intractably difficult to derive budgets governing coherent structures that are obtained using traditional eddy detection methods such as Okubo-Weiss. This is because the mask used to partition the flow into different structures is itself an implicit (and complex) function of the flow.

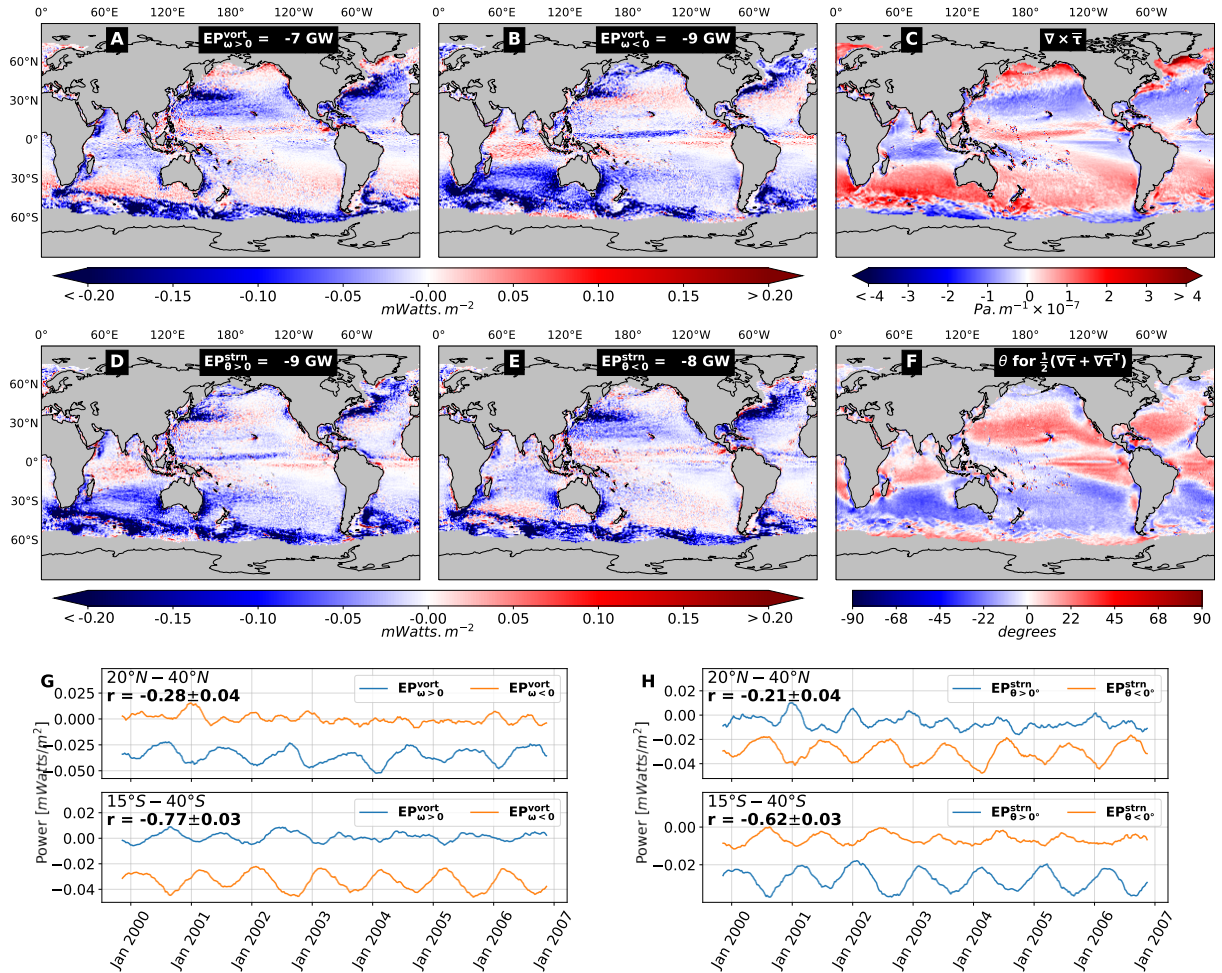


Fig. S3: Okubo-Weiss is poor at detecting the inherent asymmetry of energy transfer. Similar to Fig 3, but using Okubo-Weiss to partition the flow into [A-B] vorticity and [D-E] strain regions using a mask function. After calculating EP_ℓ from eq. (1), the mask projects EP_ℓ onto regions of [A] positive vorticity, [B] negative vorticity, [C] positive strain, and [D] negative strain regions. As in Fig 3, positive/negative polarity of strain is based on the angle θ of the local strain's diverging arm (Fig. 2F). Compared to the corresponding panels in Fig. 3, the panels here are washed out due to the binary nature of the Okubo-Weiss criterion described in the previous Fig. S2. This is clear from the energization time-series in [G], where negative vorticity in the NH (orange) and positive vorticity in the SH (blue) oscillate around zero in contrast to the corresponding plots in Fig. 3, which are clearly positive and indicate energization of anticyclonic flow by winds in the subtropics. Also missing from [G-H] here is the regular seasonal signal we saw clearly in Fig. 3 along with a significantly weaker correlation coefficients r , which is because a vorticity-dominated region as detected by Okubo-Weiss can also have significant contributions from strain of either sign and vice versa, which contaminate the time-series. Panels [C],[F] of wind stress gradients are the same as in Fig. 3.

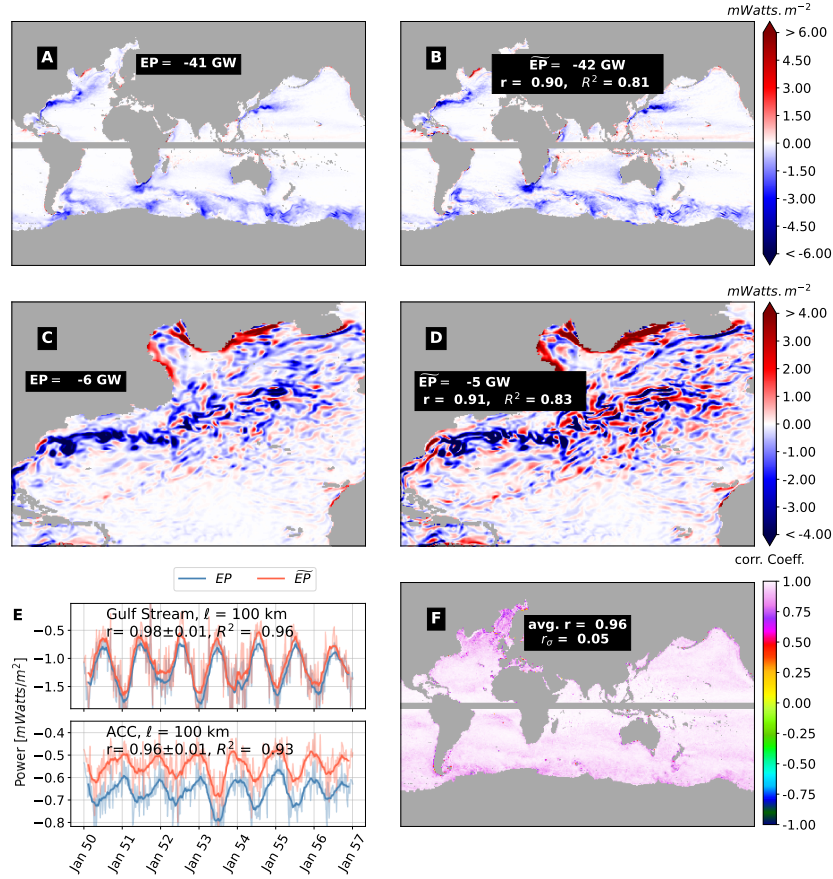


Fig. S4: CESM dataset: \widetilde{EP} is an excellent proxy for EP . Same as in Fig. 1 but using data from the high-resolution coupled ocean-atmosphere CESM simulation. [A] and [B] compare EP and \widetilde{EP} (averaged from years 50 to 56) at $\ell = 100$ km. [C] and [D] compare EP and \widetilde{EP} on a single day (Feb. 25, year 50) in the Gulf Stream region. These panels demonstrate that EP in [A],[C] can be accurately approximated by \widetilde{EP} in [B],[D], which display a high Pearson correlation coefficient $r \approx 0.9$. The coefficient of determination, $R^2 \approx 0.9$ in [B], [D], and [E] shows the fraction of the variance of EP that can be described by a linear relationship between EP and \widetilde{EP} . [A]-[D] also display the area-integrated values of EP or \widetilde{EP} (in GW). [E] shows time series of EP and \widetilde{EP} in the Gulf Stream and in the ACC, which again exhibit high correlation ($r = 0.97$ and 0.98) and demonstrates that \widetilde{EP} captures the seasonality of EP reported recently [10, 22]. Regions are defined as in [10]. [F] is a global map of the temporal correlation between EP and \widetilde{EP} at every location, and shows an average correlation coefficient $r = 0.96$ ($r_\sigma = 0.05$ is its standard deviation), which reinforces our treatment of \widetilde{EP} as an accurate proxy for EP . The $\pm 3^\circ$ gray strip at the equator is masked out since we don't calculate the geostrophic ocean velocity there.

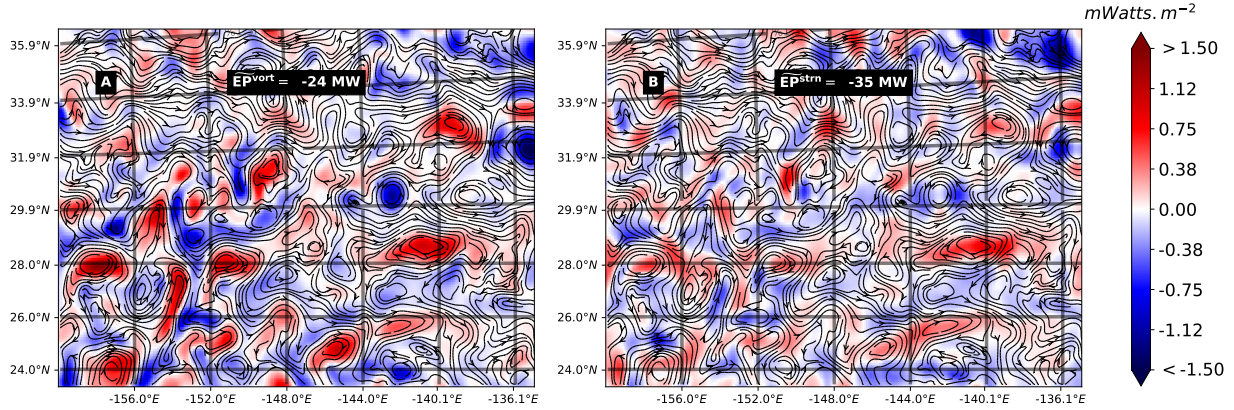


Fig. S5: CESM dataset: Disentangling Ocean Weather Energization by Winds. Same as in Fig. 2A-B, but using data from the high-resolution coupled ocean-atmosphere CESM simulation. Energy transfer (in Watts) from atmospheric winds into ocean [A] vorticity, \widetilde{EP}^{vort} and [B] strain, \widetilde{EP}^{strn} , can be analyzed for the first time using our theory and are shown here in a region in the north Pacific on Feb. 25, simulation year 50. Streamlines in [A] and [B] are identical and visualize the ocean surface currents. While vortical and straining motions always co-exist at every location, some regions can be dominated by one or the other. Demonstrating our approach, [A] shows that wind work on vorticity is most pronounced inside ocean eddies (closed streamline contours), whereas [B] shows that wind work on strain has comparable magnitude but dominates in saddle-like regions outside eddies. Ocean-induced WSGs alone always damp ocean currents and do not explain the positive wind forcing (red) in [A] and [B]. This is explained by inherent wind gradients, which naturally arise in our theory, with an important component being due to the prevailing trade winds and westerlies sketched in Fig. 2F. These lead to asymmetric energization of ocean weather based on the polarity of vortical (anti/cyclonic) and straining ($\theta > 0/\theta < 0$) flows. Straight green lines are latitude and longitude lines from the tripolar CESM grid.

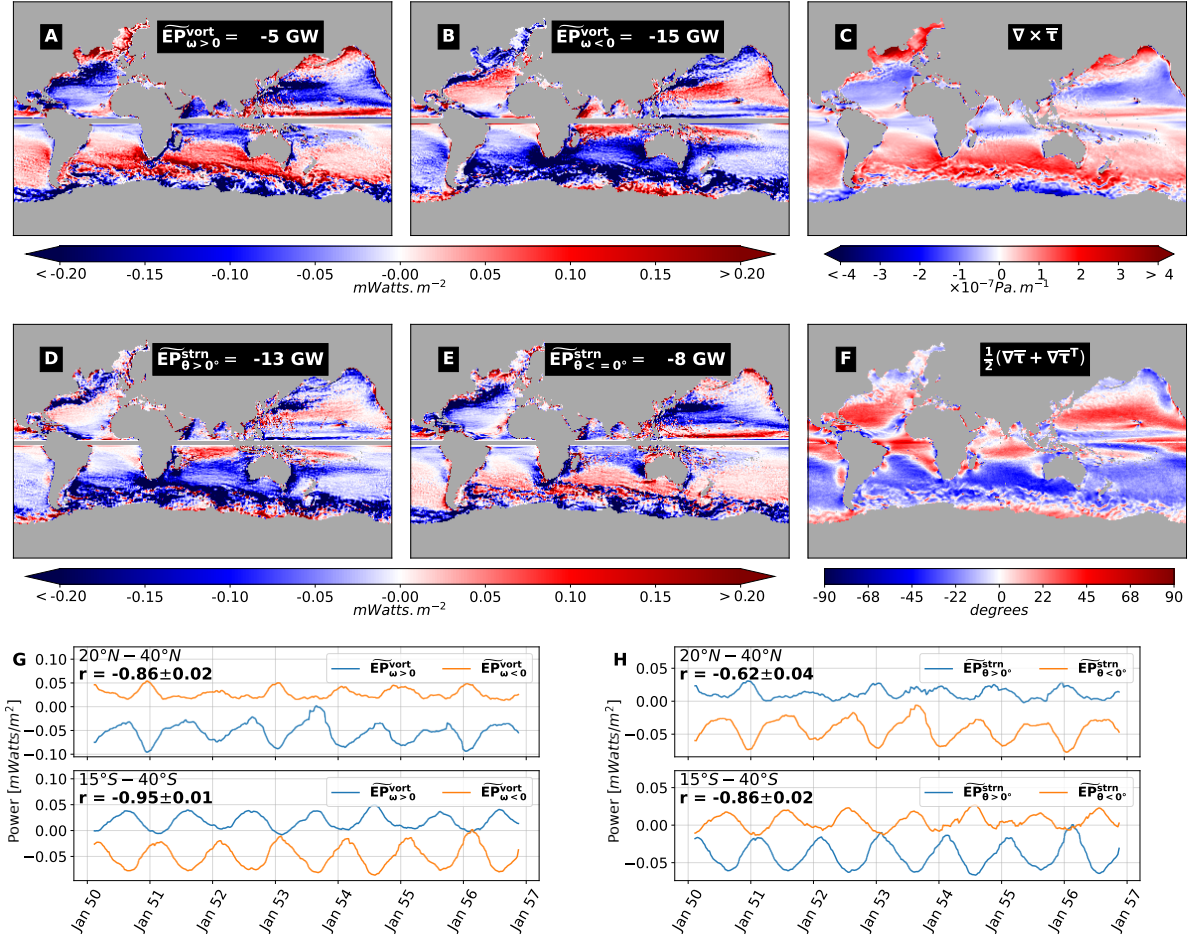


Fig. S6: CESM dataset: Unravelling Inherent Asymmetry of Energy Transfer from Winds to Ocean Weather. Same as in Fig. 3, but using data from the high-resolution coupled ocean-atmosphere CESM simulation. Top/Bottom row shows the inherent asymmetry in wind energization of vortical/straining ocean mesoscale flows. [A]/[B] is wind work on flows with positive/negative (anti/clockwise) vorticity. In the subtropics ($[15^\circ - 45^\circ]$), cyclonic/anti-cyclonic vortices are damped/energized (blue/red) by winds and the reverse occurs in sub-polar regions. While eddy-damping dominates on a global average (Fig. 1A-B), anticyclonic vortical flows are in fact energized due to inherent wind stress gradients (WSGs) in most of the subtropical oceans, except in strong current regions where the eddies are sufficiently strong such that induced WSGs, which always oppose ocean currents, dominate. [C] is a map of the time-mean wind stress curl component of inherent WSGs acting on the ocean's mesoscales. Comparing [A-B] to [C] demonstrates the prevailing winds' imprint (see Fig. 2F) on the ocean's mesoscale vortical flow. [D-E] show wind energization of straining ocean flows with a positive/negative polarity ([D]/[E]) based on the angle θ of the local strain's diverging arm (Fig. 2F). [F] is the time-mean angle of the straining WSG, which again demonstrates the prevailing winds' imprint (see Fig. 2F) on the ocean's mesoscale straining flow. [G] is a (13 weeks running mean) time series of energization of flows with positive/negative vorticity (blue/orange) at latitudes $20^\circ N - 40^\circ N$ and $15^\circ S - 40^\circ S$, excluding strong current regions analyzed in [10] where damping by induced WSGs dominates (see Methods). There is clear seasonality in [G] with the vortical flow's energization/damping peaking during the local winter. [H] is similar to [G] but for the straining mesoscale ocean flow, which shows much the same seasonality. Coarse-graining in [A-H] is at scale $\ell = 100 \text{ km}$. The $\pm 3^\circ$ gray strip at equator is masked out since we don't calculate the geostrophic ocean velocity there.

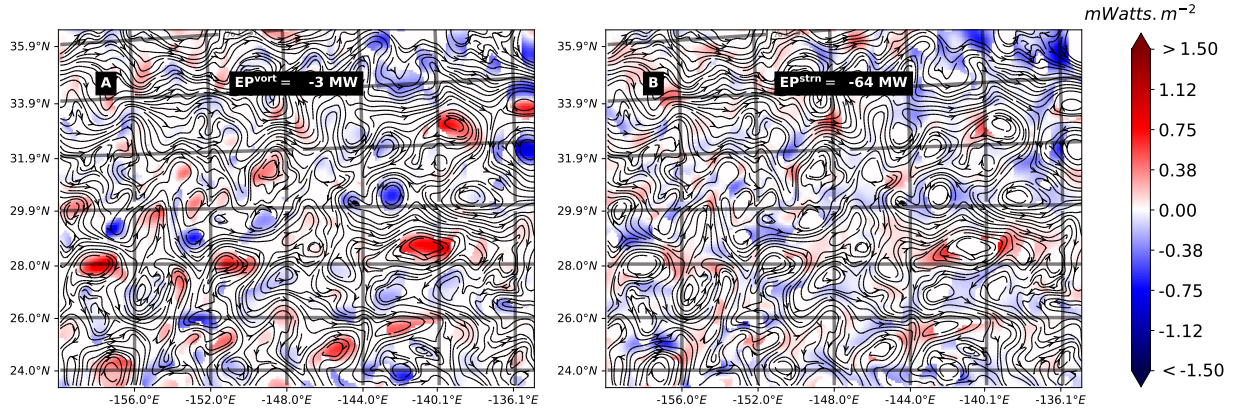


Fig. S7: CESM dataset: Using Okubo-Weiss to decompose energy transfer to vorticity and strain.. Similar to Fig. S5, but using the Okubo-Weiss criterion to partition the flow into [A] vorticity and [B] strain regions using a mask function. After calculating EP_ℓ from eq. (1), the mask projects EP_ℓ onto [A] vorticity-dominated and [B] strain-dominated regions. On one hand, this figure provides support to our approach by showing results that are qualitatively consistent with Fig. 2A-B. However, as we found in Fig. S2 from the satellite dataset, the panels here are washed out due to the binary nature of the Okubo-Weiss criterion and highlights shortcomings of traditional approaches based on eddy detection. In [A], damping of vorticity is severely underestimated (-3 MW); it is only 15% of the energy transfer revealed by our approach in Fig. S5A (-20 MW). On the other hand, energization of strain in [B] is significantly underestimated compared to Fig. S5B leading to a bulk strain damping (-64 MW) that is more than twice the damping in (-30 MW). Most importantly, it is intractably difficult to derive budgets governing coherent structures that are obtained using traditional eddy detection methods such as Okubo-Weiss. This is because the mask used to partition the flow into different structures is itself an implicit (and complex) function of the flow.

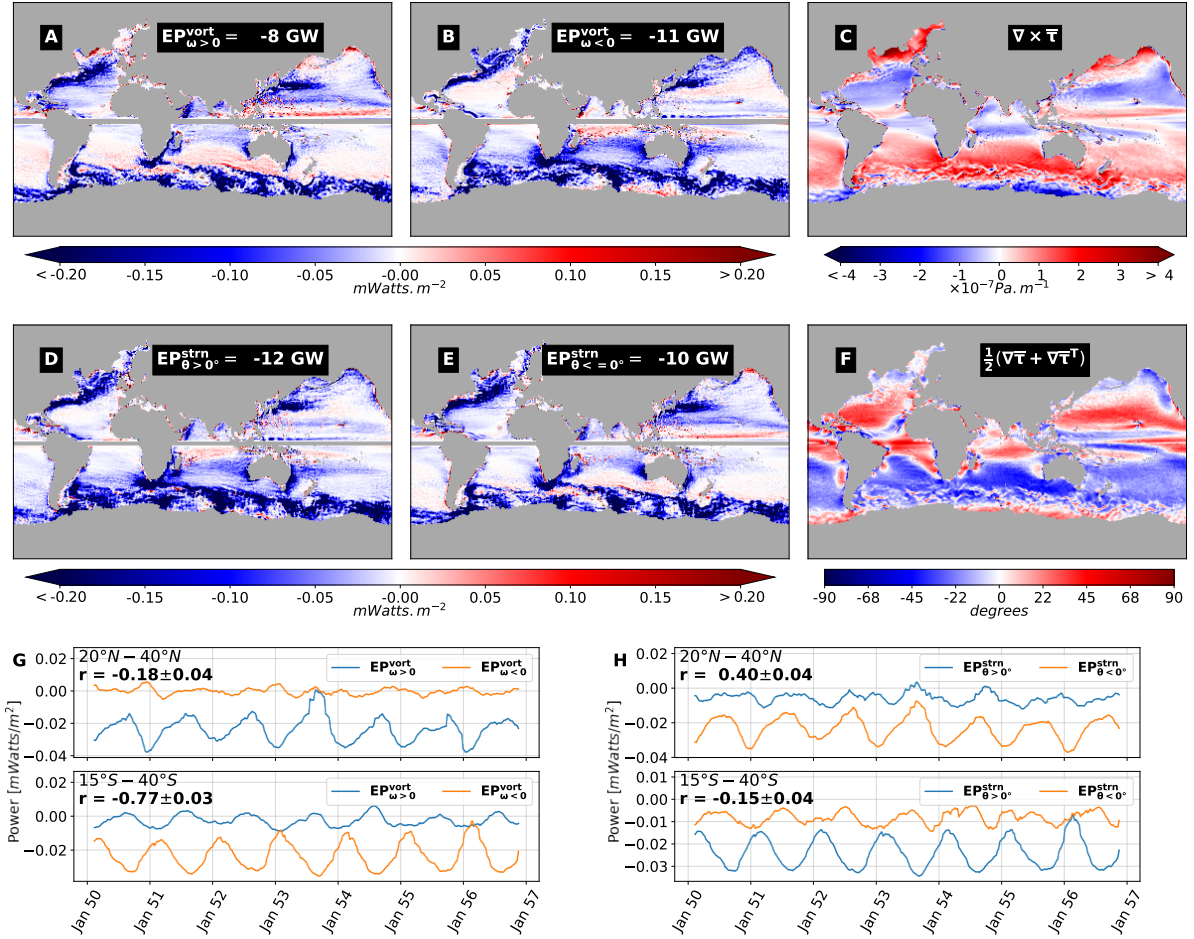


Fig. S8: CESM dataset: Showing the Okubo-Weiss is poor at detecting the inherent asymmetry of energy transfer. Similar to Fig S6, but using Okubo-Weiss to partition the flow into [A-B] vorticity and [D-E] strain regions using a mask function. After calculating EP_ℓ from eq. (1), the mask projects EP_ℓ onto regions of [A] positive vorticity, [B] negative vorticity, [C] positive strain, and [D] negative strain regions. As in Fig S6, positive/negative polarity of strain is based on the angle θ of the local strain's diverging arm (Fig. 2F). Compared to the corresponding panels in Fig. S6, the panels here are washed out due to the binary nature of the Okubo-Weiss criterion described above in Figs. S2,S3,S7. This is clear from the energization time-series in [G], where negative vorticity in the NH (orange) and positive vorticity in the SH (blue) oscillate around zero in contrast to the corresponding plots in Fig. S6, which are clearly positive and indicate energization of anticyclonic flow by winds in the subtropics. Also missing from [G-H] here is the regular seasonal signal we saw clearly in Fig. S6 along with a significantly weaker correlation coefficients r , which is because a vorticity-dominated region as detected by Okubo-Weiss can also have significant contributions from strain of either sign and vice versa, which contaminate the time-series. Panels [C],[F] of wind stress gradients are the same as in Fig. S6.

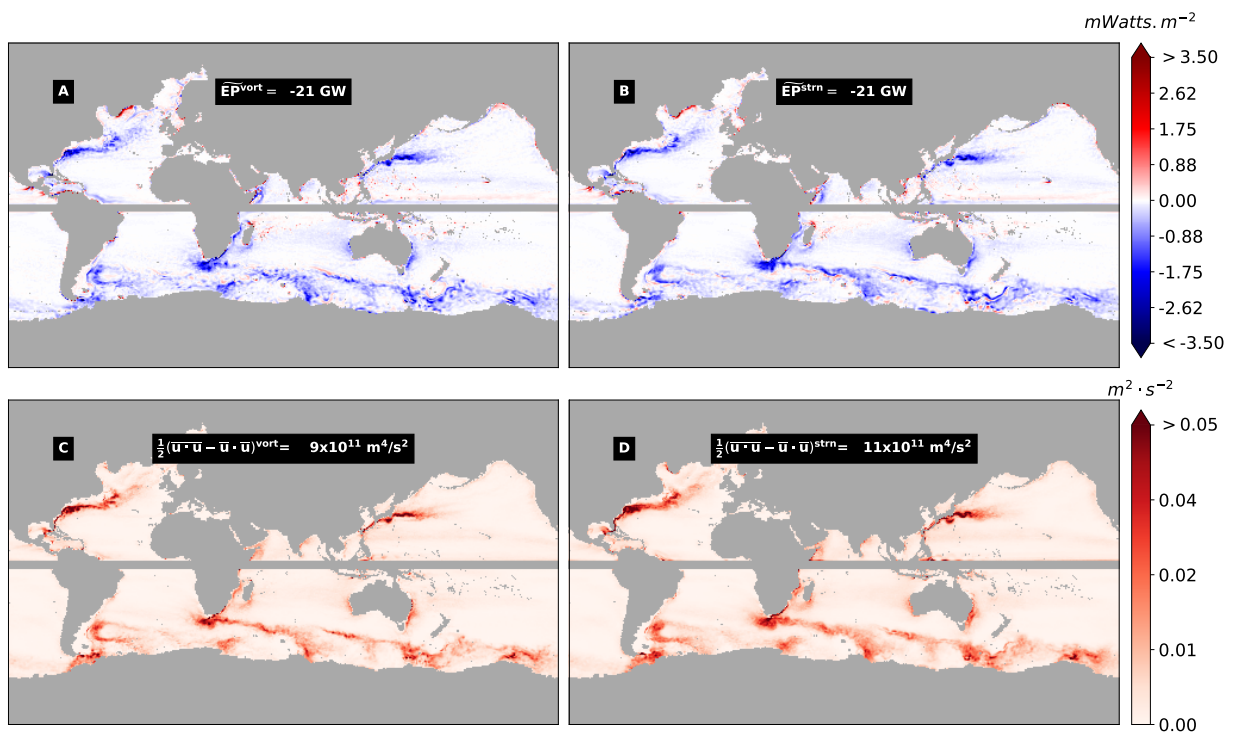


Fig. S9: CESM dataset: Wind damping of mesoscale strain and vorticity.. Similar to Fig. S1 but using CESM data, for completeness.

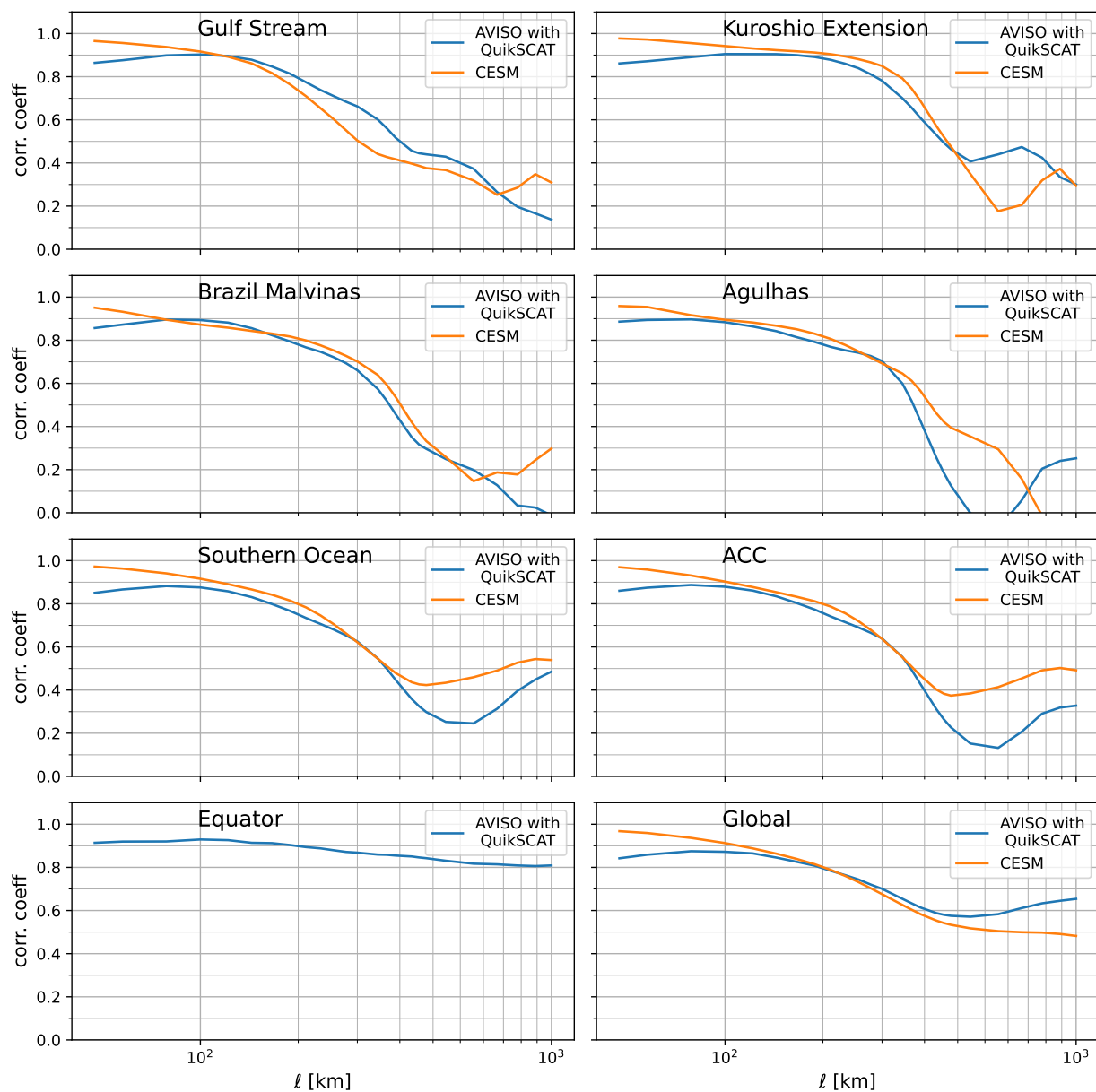


Fig. S10: \widetilde{EP}_ℓ is an accurate proxy for EP_ℓ at scales ℓ smaller than ≈ 200 km. As discussed in the Main text and in the Methods, the extent to which \widetilde{EP}_ℓ is an accurate proxy for EP_ℓ depends on the latter’s ultraviolet locality. Ultraviolet locality of EP_ℓ does not hold at scales around the mesoscale spectral peak ($\ell \approx 300$ km) and larger (see [2, 42]). Panels here plot the correlation between EP_ℓ and \widetilde{EP}_ℓ , which show that indeed \widetilde{EP}_ℓ becomes a poor approximation at those larger scales. An exception is the Equator, where there is no mesoscale spectral peak (see Fig. 1 in [42]). Blue/orange plots show correlation using the satellite/model datasets. Correlation coefficients shown here use single time snapshots shown in Fig 1 [C][D] and S4[C][D]. The Equator does not show CESM data since we don’t calculate the geostrophic ocean velocity from CESM within the band $\pm 3^\circ$.